A Synthetic Aperture Radar Imaging Mode Utilizing Frequency Scan for Time-of-Echo Compression

Marwan Younis, *Fellow, IEEE*, Felipe Queiroz de Almeida, Tobias Bollian, *Member, IEEE*, Michelangelo Villano, *Senior Member, IEEE*, Gerhard Krieger, *Fellow, IEEE*, and Alberto Moreira, *Fellow, IEEE*

***Abstract*— The synthetic aperture radar (SAR) imaging mode described in this article utilizes the available signal bandwidth to form a narrow frequency-scanning transmit antenna beam illuminating the swath of interest from far to near range. The imaging technique is named frequency scan for time-of-echo compression (f-STEC), because, for a proper choice of mode parameters, the radar echo duration is reduced, i.e., compressed. This article provides a detailed analysis of the f-STEC imaging technique and derives the operational and performance parameters as well as—to the authors' knowledge—for the first time, analytic expressions for the f-STEC timing constraints. Furthermore, the performance and trade space are reported and compared to both conventional and modern, i.e., digital beamforming imaging modes. The f-STEC imaging technique is shown to be specifically advantageous for SAR systems operating at higher carrier frequencies or an attractive add-on for state-of-the-art SAR instruments.**

***Index Terms*— Frequency scaning radar, imaging radar, performance analysis, radar imaging techniques, spaceborne radar, synthetic aperture radar (SAR).**

I. Introduction

THE development of synthetic aperture radar (SAR) instruments at higher carrier frequency, such as Ka-band [1], [2], [3], [4], [5], is motivated, among others, by the relative wavelength scaling, which provides an increased bandwidth and reduced physical dimensions of the RF front end. The difficulty in the realization of high-performance [here, in terms of swath width, azimuth resolution, and signal-to-noise ratio (SNR)] spaceborne SAR sensors at Ka-band and beyond is traced back to two main reasons.

1) Operating in conventional imaging modes leads to a small antenna area—possibly even violating the minimum antenna area constrain [6]—of extremely large length-to-height aspect ratio.
2) The RF technology for multichannel SAR allowing for the use of digital beamforming techniques—which would overcome the former difficulties [7]—is not yet available.

Manuscript received 24 May 2022; revised 21 September 2022; accepted 26 October 2022. Date of publication 17 November 2022; date of current version 8 December 2022. *(Corresponding author: Marwan Younis.)*

The authors are with the Microwaves and Radar Institute, German Aerospace Center (DLR), 82234 Weßling, Germany (e-mail: marwan.younis@dlr.de).

Digital Object Identifier 10.1109/TGRS.2022.3223032

To elaborate on the reason, consider increasing the carrier frequency of the SAR instrument while keeping the imaged swath width fixed. The consequence of the smaller antenna area is a degradation of the SNR at the receiver, even if the peak transmit power, and by this the power density on the ground, is maintained constant. This is because of the reduced receive power due to the reduced effective antenna area [8], [9], [10]. The high antenna aspect ratio is problematic from an electrical design and mechanical stability point of view. Thus, shortening the antenna length may be favorable and comes with the beneficial side effect of allowing for an improved azimuth resolution [11], but it causes a further SNR degradation and a reduced swath width [6], [7].

The dilemma could be overcome by the use of digital beamforming techniques such as SCan-On-REceive (SCORE) [7], [9], [12], [13], [14]. However, the technology for these systems is one major reason preventing high-performance high-frequency SAR [3], [15], [16], [17], [18]. In summary, the realization of spaceborne SAR at Ka-band frequencies and above poses serious constraints but may be circumvented through the imaging technique described here.

Frequency-scanning antennas and radar systems have been known for a long time and are utilized, for example, in automotive radar [19], [20]. The imaging mode described hereafter is known in a general form as f-Scan in [21], [22], and [23]; further work focusing on the processing and the data compression has been published in [24] and [25], respectively. A recent publication on f-SCAN can be found in [26]. In line with the new contributions of this article, the imaging mode is (re)named to frequency scan for time-of-echo compression (f-STEC), aiming to emphasize the echo compression characteristic that will be shown to be an essential element of the imaging mode, relative to the frequency-scanning antenna property.[1]

The f-STEC mode has the potential to eliminate the above-mentioned problems when moving to higher frequency SAR by exploiting the available trade-space parameters. Specifically, it is shown that f-STEC trades (sacrifices) range resolution for (improved) SNR while leading to a moderate antenna area aspect ratio. Furthermore, the beam-scanning

[1]In fact, when utilizing chirp signals, the frequency scanning becomes obsolete as it can be replaced by a time-varying transmit antenna beam.

parameters of the technique may be chosen to significantly reduce the duration of the radar echo window without sacrificing swath width. This is a major advantage of the f-STEC imaging technique, which can be traded for a longer transmit pulse duration and lower peak-to-average power ratio. At the same time, f-STEC is also advantageous as a possible add-on imaging mode for upcoming lower frequency SAR missions offering sufficient bandwidth [27].

The basic concept behind the f-STEC imaging mode is straightforward and consists of three key aspects.

1) Transmitting a frequency-modulated signal.
2) The steering angle of the antenna's main beam is a function of frequency.
3) The main beam scans the imaged swath from far to near range.

The angular direction of the radiation pattern's main lobe (referred to as main beam) of a frequency-scanning antenna is a function of the signal's RF frequency. Thus, f-STEC utilizes the available bandwidth to form a narrow frequency-scanning transmit antenna beam illuminating the swath of interest from far to near range. The frequency-scanning receive antenna beam then collects the (compressed) return echo signal reflected from the ground. The scan direction is a prerequisite to yield compression of the echo window length, i.e., the duration of the radar return echo from the ground, which would not occur when scanning from near to far range.

Several options exist for the realization of such an antenna, ranging from passive leaky wave antennas [28] to active phased array antennas where the frequency dependence is imposed by the transmit/receive modules or a reflector antenna combined frequency dispersive feed array. The latter is shown in Fig. 1 for the simplified case of four color-coded frequencies; here, all feed elements illuminate the complete reflector surface and the different feed element positions result in reflector beams pointing to a different direction.

This article is organized as follows. The f-STEC operation principle is introduced in Section II and compared to other imaging techniques. In Section III, the parameters governing f-STEC operation are introduced together with the equations describing these parameters. Signal timing and echo window length, elaborated in Section IV, are important for determining the extent and position of the imaged swath. Section V derives the SNR equations for f-STEC and two other operation modes; the performance of these systems is then compared to each other in Section VI. Finally, Section VII summarizes the f-STEC operation mode and points out further aspects to be investigated.

II. Frequency Scan for Time-of-Echo Compression

Spaceborne SAR instruments typically transmit pulsed signals of constant envelope and linearly varying instantaneous frequency, known as chirps. Utilizing a frequency-scanning antenna, the instantaneous frequency variation of the chirp over time translates into a changing direction of the antenna's main beam over time. For f-STEC, the (half power) beamwidth is smaller than the angular swath extent. The frequency-varying (narrow) beam direction thus scans the swath and

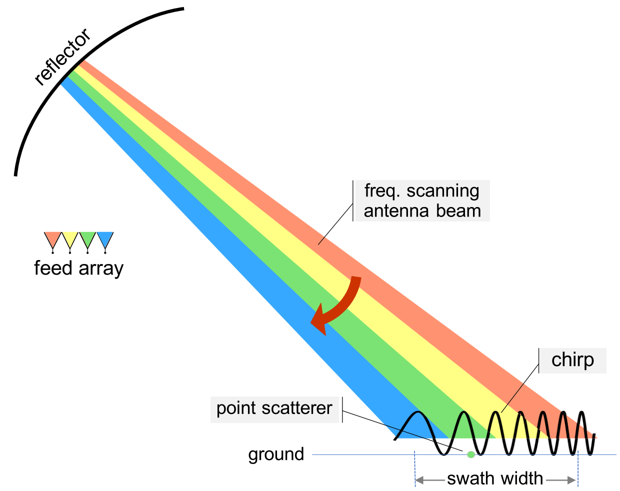

Fig. 1. Illustration of f-STEC operation principle realized by a reflector antenna and a frequency dispersive feed array. Here, for simplicity, only four discrete color-coded frequencies are assumed each radiated by a distinct feed element resulting in a narrow output antenna beam.

can be thought of as a spatial and temporal spreading of the signal's frequencies over the swath angles. This is shown in Fig. 1 for the simplified case of four discrete frequencies, each radiated by one antenna element of the feed array. When exciting the feed array by a chirp waveform, the radiation center changes with time and frequency along the feed array, which effectively scans the reflector beam.

It is necessary to understand that the abovementioned scanning property is a consequence of the frequency-modulated (chirp) signal in conjunction with the dispersive antenna, but not an intrinsic property of the antenna itself. Each spectral component of the signal at the terminals of the antenna generates its own narrow beam; if all spectral components were imposed simultaneously, then all corresponding antenna beams would also be generated simultaneously. The technique should not be confused with that of frequency diverse antenna arrays, addressed, for example, in [29] and [30], which, although similar, are not suitable for f-STEC as described here.

The transmit (Tx) and receive (Rx) radiation patterns of a passive antenna are identical as a consequence of the reciprocity of Maxwell's equations and electromagnetic theory within an isotropic medium [28], [31]. Assuming that the same antenna is used for transmission and reception implies that, on-receive, the antenna's main beam will inherently point to the direction of the ground echo. Again, the radiation pattern can be thought of as consisting of many (overlapping) main lobes, each pointing to the distinct direction of the corresponding frequency. This can be understood as the antenna collecting the signal frequencies that have previously been spread over the imaged swath.

To summarize, exciting a chirp signal at the terminals of a frequency-scanning antenna will generate a narrow transmit beam scanning the swath over time. The linearity of electromagnetic scattering causes the echo signal to maintain the frequency of the incident wave. Consequently, the receiving radiation pattern's narrow main lobe is instantaneously pointing toward the echo direction independently of its time of arrival.

On a first view, f-STEC may seem similar to the SCORE [12], [13], [14], [32] operation mode. This is, however, misleading as there are substantial differences.

1) *Transmit Pattern:* SCORE generates a fixed, wide, and low-gain radiation pattern illuminating the complete swath with the full signal bandwidth, while f-STEC utilizes a time-dependent narrow and high-gain pattern scanning over the swath.
2) *Receive Pattern:* In SCORE, the antenna array's (digital) excitation coefficients are controlled to generate a narrow pattern that follows the pulse echo on the ground, while in f-STEC, the fixed but frequency-dependent radiation patterns are inherently generated by the antenna, where each beam is pointing to the direction of an incoming monochromatic wave.
3) *Timing:* The duration of the ground echo is primarily proportional to the swath width (geometry) in SCORE, and thus, imaging a wider swath will increase the echo duration. For f-STEC, the echo duration is an operational parameter (cf. Section IV-B), and its minimum value can be a fraction of the transmitted chirp and shorter than the corresponding swath width.

III. Imaging Mode Parameters

In the following, we proceed by developing equations that describe the mode parameters assuming ideal, i.e., simplified conditions and by this accentuating the trade space. The developed equations may be used to provide a quantitative instrument design and operational parameter values. At this point, it is sufficient to consider the 2-D incidence plane geometry. The antenna beamwidth in elevation, Θ_{el}, is assumed to be equal to the radiation pattern's half-power beamwidth and, for simplicity, independent of the scan angle and is given by

$$\Theta_{\mathrm{el}} = \gamma_{\mathrm{el}} \frac{\lambda}{h_{\mathrm{ant}}} \tag{1}$$

where λ is the carrier wavelength, h_{ant} is the antenna height (in cross-track direction), and γ_{el} is a constant of proportionality, which depends mainly on the antenna type, taper, and illumination.

A. Dwell Bandwidth and Dwell Time

The two main performance parameters are the dwell time and the dwell bandwidth that are defined as the duration during which a point target is illuminated by a single radar transmit pulse and the range of frequencies (bandwidth) seen by the point target during that time, respectively.

With reference to Fig. 2, the angular swath extent is denoted by $\Theta_{\mathrm{sw}} = \theta_{\mathrm{far}} - \theta_{\mathrm{near}}$, while the available signal (system) bandwidth is $B_{\mathrm{sys}} = |f_e - f_s|$ with the instantaneous carrier frequencies f_s and f_e at the start and end of the chirp, respectively. Since the direction (i.e., scan angle) of the antenna's main beam is determined by the signal frequency, there is a one-to-one correspondence between the instantaneous frequency and the beam scan angle. Specifically, at chirp start time, the instantaneous frequency is f_s and the main beam points to θ_s, as shown in Fig. 2, whereas at chirp frequency f_e, the beam maximum points to θ_e. Here, the angles are measured with respect to an arbitrary reference, taken to be the nadir direction. At this point, no explicit assumption has been made as to whether an up chirp $f_s < f_e$ or a down chirp $f_s > f_e$ is transmitted, thus not implying the time dependence of the scan direction, which is irrelevant for the operation parameters derived next.

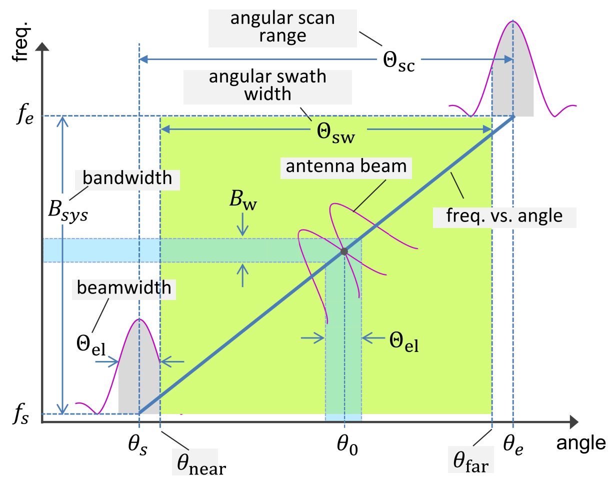

Fig. 2. Illustration of frequency scan for a linear correspondence between RF frequency and scan angle. The variation of the scan direction with instantaneous frequency leads to a distribution (dispersion) of the available bandwidth over range.

To ensure that each point within the swath is traversed by the complete antenna beamwidth, it is necessary that the angular scan extent $\Theta_{\mathrm{sc}} = |\theta_e - \theta_s|$ is larger than the angular swath extent by an amount equal to the antenna beamwidth, and thus,

$$\Theta_{\mathrm{sc}} = |\theta_e - \theta_s| = \Theta_{\mathrm{sw}} + \Theta_{\mathrm{el}} \tag{2}$$

where $|\cdot|$ indicates the absolute value introduced here to ensure a correct expression for all $\theta_s \gtrless \theta_e$.

A closed expression can be derived by assuming a linear dependence[2] between the scan angle θ and the instantaneous frequency f, cf. straight line in Fig. 2, which is given by

$$f = f_s \pm B_{\mathrm{sys}} \frac{|\theta - \theta_s|}{\Theta_{\mathrm{sc}}} \tag{3}$$

where $+$ and $-$ correspond to an up and down chirp, respectively.

To determine the dwell bandwidth, B_w, consider a point on the ground at angular position θ_0. The instantaneous frequencies f_a and f_b at the edges of the beamwidth, i.e., when the antenna beam moves into and out of the point, are obtained by inserting $\theta = \theta_0 \pm \Theta_{\mathrm{el}}/2$ into (3) yielding

$$\begin{aligned} f_a &= f_s \pm B_{\mathrm{sys}} \frac{|\theta_0 - \frac{\Theta_{\mathrm{el}}}{2} - \theta_s|}{\Theta_{\mathrm{sc}}} \\ f_b &= f_s \pm B_{\mathrm{sys}} \frac{|\theta_0 + \frac{\Theta_{\mathrm{el}}}{2} - \theta_s|}{\Theta_{\mathrm{sc}}} \end{aligned} \tag{4}$$

respectively, from which the dwell bandwidth (cf. Fig. 2) is readily obtained as

$$B_w = |f_b - f_a| = \frac{\Theta_{\mathrm{el}}}{\Theta_{\mathrm{sc}}} B_{\mathrm{sys}} \tag{5}$$

[2] In general, the scan angle will be a monotonously increasing (or decreasing) function of frequency and time depending on the specific antenna system realization.

which, when reformulated by inserting (2) finally gives[3]

$$B_w = \frac{B_{\text{sys}}}{\frac{\Theta_{\text{sw}}}{\Theta_{\text{el}}} + 1}. \tag{6}$$

Although simple, the above expression describes the parameters of the frequency scan technique and is worth understanding. The dwell bandwidth—which determines the range resolution—is proportional to, but smaller than the total (invested) signal bandwidth. The denominator of (6) is larger than 1 by an amount equal to the ratio of angular swath extend to beamwidth; thus, increasing either the imaged swath width or the antenna height h_{ant} will reduce the dwell bandwidth. This shows the main trade space of the f-STEC imaging mode to be range resolution versus swath width and SNR, and the latter is determined by the antenna gain, which is proportional to the antenna height (see Section V). The ratio $\Theta_{\text{sw}}/\Theta_{\text{el}}$ can be understood as the number of beamwidths necessary to cover the swath. This is a static quantity, as is the expression in (6) in the sense that it does not involve the beam scanning rate, which thus does not affect the dwell bandwidth and has therefore not been considered up to now.

The trade space described by (6) is shown in Fig. 3. The left ordinate represents the dwell-to-chirp bandwidth, $\gamma_w = B_w/B_{\text{sys}}$, where γ_w is the dwell factor, in percent versus the abscissa taken to be the f-STEC antenna height normalized to the height of a stripmap SAR antenna imaging the same swath. Note that the height of a stripmap SAR antenna is readily obtained by inserting Θ_{sw} into (1), in which case the two-way pattern will be 6 dB below the maximum at the swath edges. Increasing the antenna height increases its gain without decreasing the swath width (as in stripmap mode), but it also reduces the antenna beamwidth, and by this, the spectral support of a point target positioned within the swath. As such, the underlying trade is SNR versus range resolution.

The right ordinate of Fig. 3 represents the swath-to-beamwidth ratio, $\Theta_{\text{sw}}/\Theta_{\text{el}}$, introduced earlier. The line has a slope of 1 for identical f-STEC and stripmap antenna types, which can be easily verified by inserting (1).

Next, the dwell time duration, defined earlier as the time during which a point target on the ground is illuminated, is derived. Define the pulse start and end times (leading and lagging pulse edge, respectively) by t_1 and $t_1+\tau_p$, respectively, where $\tau_p > 0$ is the pulse duration. By following the exact same procedure leading to the dwell bandwidth, we arrive at the expression relating the scan angle and the time:

$$t = t_1 + \tau_p \frac{|\theta - \theta_s|}{\Theta_{\text{sc}}} \tag{7}$$

which, following the same reasoning as before, leads to the expression for the dwell time:

$$\tau_w = \frac{\tau_p}{\frac{\Theta_{\text{sw}}}{\Theta_{\text{el}}} + 1}. \tag{8}$$

Note that the dwell factor, γ_w, describes the ratio of dwell-to-pulse duration as well as dwell-to-system bandwidth

$$\gamma_w = \frac{\tau_w}{\tau_p} = \frac{B_w}{B_{\text{sys}}} = \frac{1}{\frac{\Theta_{\text{sw}}}{\Theta_{\text{el}}} + 1} = \frac{\Theta_{\text{el}}}{\Theta_{\text{sc}}}. \tag{9}$$

[3]An equivalent expression is stated in [21] and [22].

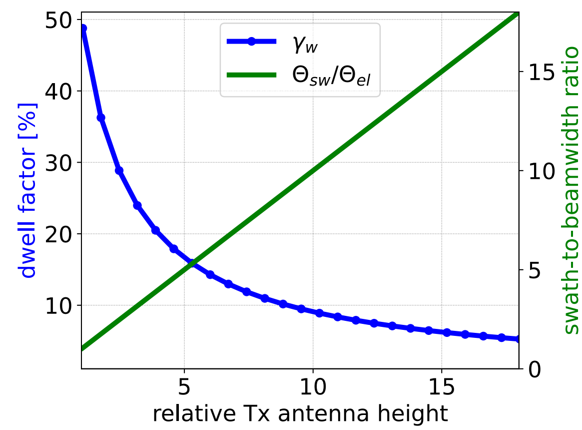

Fig. 3. Percentage dwell factor (left ordinate) and the ratio of the angular swath extent to antenna pattern beamwidth (right ordinate) plotted versus the antenna height normalized to the height of a stripmap antenna imaging the same swath width.

Fig. 3 thus also shows the percentage dwell-to-pulse duration as a function of normalized antenna height. Comparing (8) to (6) shows an identical form of dependence for the dwell time and dwell bandwidth, which justifies the identical curves for the two quantities. The implication, however, is rather different: a reduced dwell bandwidth is advantageous in terms of SNR since it reduces the noise power,[4] while the opposite is true for the dwell time, since a reduced point target illumination time reduces the average power density and, by this, causes a reduced SNR. In Section V, an expression for the SNR is developed, which quantifies the dependence on the various parameters.

An interesting effect occurs when the beamwidth converges toward the angular swath extent, i.e., $\Theta_{\text{el}} \to \Theta_{\text{sw}}$. One would expect that the dwell bandwidth and dwell time converge to the signal bandwidth and pulse duration, respectively as is the case for classical stripmap operation. This is, however, not the case (!) as shown in Fig. 3 where the percentage dwell factor approaches 50% when the f-STEC and stripmap antenna heights become equal. The reason is inherent to the f-STEC operation since the beam is (still) scanned with the start/end steer angle lying outside the swath. Mathematically, this manifests itself through additive 1 in the denominator of (9) such that

$$\gamma_w \Big|_{\Theta_{\text{el}} \to \Theta_{\text{sw}}} = \frac{1}{2}. \tag{10}$$

From (2), it is evident (cf., also Fig. 2) that in this case, $\Theta_{\text{sc}} = 2 \cdot \Theta_{\text{el}} = 2 \cdot \Theta_{\text{sw}}$. The above scenario indicates the least favorable operation or, stated differently, an efficient f-STEC manifests itself by a large swath-to-beamwidth ratio $\Theta_{\text{sw}}/\Theta_{\text{el}} \gg 1$.

One important aspect worth noting is the shape of the antenna's radiation pattern, which manifests itself through the relation between the assumed beamwidth, Θ_{el}, and the half-power beamwidth. The temporal and spectral response to a point target is determined by the shape of the radiation pattern, which affects the main performance parameters such as the

[4]The noise power is proportional to kTB_w, where k is Boltzmann's constant and T is the temperature in kelvin.

dwell bandwidth and time and, by this, determines the impulse response function.

B. Echo Time Reversal

To derive the condition for the echo time reversal, the geometry and timing are considered in detail. At this point, the earlier assumption of arbitrary scan direction is dropped and the antenna's main beam radiation pattern is specified to scan from far to near range, i.e., $\theta_e < \theta_s$.

Take as reference a sphere centered at the antenna and just large enough to contain the complete antenna structure. Let t_1 and $t_1 + \tau_p$ mark the time instances where the leading and lagging "edge" of an electromagnetic wave generated by a transmitted pulse of duration τ_p passes the sphere.

The aim is to determine the time of arrival of various "portions" of the transmit pulse ground echo. This can best be calculated by considering a Dirac delta impulse transmitted at time $t = t_1 + \Delta t$, where $0 \le \Delta t \le \tau_p$. The steering direction of the beam center, i.e., the maximum of the antenna's radiation pattern, as a function of time is determined by solving (7) for $\theta_0(t)$—the subscript $_0$ is added to indicate the beam center—yielding

$$\theta_0(t) = \theta_s - \frac{\Theta_{\text{sc}}}{\tau_p}(t - t_1) = \theta_s - \frac{\Theta_{\text{sc}}}{\tau_p}\Delta t \tag{11}$$

where, as expected, the scan limits are θ_s and θ_e at times $\Delta t = 0$ and τ_p, respectively. To determine the time delay, τ_h, after which the beam-center points to the far-range angle of the swath, set $\theta_0(\tau_h) = \theta_{\text{far}}$ and solve (11) for $\Delta t = \tau_h$, and thus,

$$\begin{aligned} \theta_0(t)\big|_{\Delta t=\tau_h} &= \theta_{\text{far}} \\ \Rightarrow \tau_h &= \frac{\Theta_{\text{el}}}{\Theta_{\text{sc}}}\frac{\tau_p}{2} = \frac{\tau_w}{2} \end{aligned} \tag{12}$$

where the last two terms in (12) have been recast in terms of the antenna beamwidth Θ_{el} introduced earlier and the dwell time from (9). The above expression is intuitively comprehensible since the dwell time is the duration any target remains within the antenna main beam; hence, after $\Delta t = \tau_w/2$ seconds, the beam center has moved by half a beamwidth and is pointing to θ_{far} corresponding to slant range R_{far}. The ground echo return will arrive at the reference sphere at time instance

$$t_{\text{far}} = t_1 + \frac{\tau_w}{2} + \frac{2R_{\text{far}}}{c_0}. \tag{13}$$

The same reasoning is used to determine the time $\Delta t = \tau_p - \tau_h$ at which the main beam is pointing toward the near range of the swath θ_{near}; the corresponding echo from slant range R_{near} will then arrive at time

$$t_{\text{near}} = t_1 + \tau_p - \frac{\tau_w}{2} + \frac{2R_{\text{near}}}{c_0}. \tag{14}$$

The f-STEC technique allows for an echo time reversal, which occurs if the far-range signal echo arrives earlier than the near-range echo. At the reversal point, both near and far-range echos arrive at the same time instance. Setting $t_{\text{far}} = t_{\text{near}}$ from (13) and (14) and substituting for τ_w from (12) yield the following condition:

$$\begin{aligned} t_{\text{far}} &= t_{\text{near}} \quad \text{for} \quad \tau_p = \tau_0 \\ &\Rightarrow \tau_0 = \frac{2}{c_0}(R_{\text{far}} - R_{\text{near}})\frac{\Theta_{\text{sc}}}{\Theta_{\text{sw}}} \end{aligned} \tag{15}$$

where τ_0 is named the intrinsic duration and depends on the swath geometry and antenna pattern beamwidth. When the duration of the transmitted pulse is equal to the intrinsic duration, both near- and far-range echoes arrive at the same time instance. The above conveys that echo time reversal, $t_{\text{far}} < t_{\text{near}}$, occurs for long transmit pulse durations and small swath widths.

The ratio of transmit-to-intrinsic pulse duration is a relevant imaging mode parameter, as it allows specifying the f-STEC operation point, defined by

$$\begin{aligned} O_p &= \frac{\tau_p}{\tau_0} = \frac{\tau_p c_0}{2(R_{\text{far}} - R_{\text{near}})}\frac{\Theta_{\text{sw}}}{\Theta_{\text{sc}}} \\ &= \frac{\tau_p c_0}{2(R_{\text{far}} - R_{\text{near}})}(1 - \gamma_w). \end{aligned} \tag{16}$$

When $t_{\text{far}} = t_{\text{near}}$, the system operates at the reversal point for which $O_p = 1$ and the echo window length is minimized as will be shown later. The system operates in echo reversal for $O_p \ge 1$, while the near-range echo arrives before the far-range echo when $O_p < 1$. Note that, as mentioned earlier, the echo window length compression is inherent to the f-STEC imaging and occurs, independently of the value of the operation point, as a consequence of the far-to-near beam scanning.

It should be pointed out that for a classical SAR, t_{far} is always larger than t_{near} such that an echo time reversal will not occur. This is because the transmitted pulse propagates as a spherical wave illuminating the swath from near to far range; a time-angle correspondence as given by (11) is not applicable. It is worth mentioning, however, that a similar echo compression can be achieved by using subpulse techniques [33], [34], [35], [36] as suggested in [37].

IV. Echo Window Timing

The imaging mode parameters presented in Section III are used in the following to compute quantities related to the timing of an SAR system operating in the f-STEC mode. A graphical representation of the timing diagram (also known as diamond diagram) is commonly used in order to determine the possible extent (width) and position of the imaged swath. The expressions for the blockage caused by the transmit pulse and the nadir return are derived after introducing the time–range equation.

A. Range–Time Characteristics

For a spherical Earth of radius r_E, there is a one-to-one correspondence between the off-nadir look angle, θ, and the slant range, which is given by (cf. e.g., [38])

$$r(\theta) = r_O \cos\theta - \sqrt{r_E^2 - (r_O \sin\theta)^2} \tag{17}$$

where $r_O = r_E + h_{\text{sat}}$ is the radius of the satellite orbit and h_{sat} is the orbit height. Consider a Dirac delta transmitted—passing the reference sphere—at time instance $t = t_1 + \Delta t$ when the beam center is scanned to $\theta_0(t)$ given by (11). Inserting into (17) yields the beam-center range as a function of time

$$r_0(t) = r_O \cos\theta_0(t) - \sqrt{r_E^2 - (r_O \sin\theta_0(t))^2}. \tag{18}$$

The return echo from range $r_0(t)$ will be received—pass the reference sphere—after a time delay $2r_0(t)/c_0$ at time

$$t_0 = t_1 + \Delta t + \frac{2r_0(t)}{c_0}. \tag{19}$$

The last two expressions give an profound insight into the f-STEC mode and are therefore considered in detail in the following. First, note that the expressions are with respect to the beam center. The slant range of the leading (or lagging) beam edge is easily obtained by subtracting (or adding) $\Theta_{\mathrm{el}}/2$ to $\theta_0(t)$ in (18). The temporal quantity corresponding to $\Theta_{\mathrm{el}}/2$ is $\tau_w/2$, as such the leading beam edge moves into the far swath at $\Delta t = 0$, while the lagging beam edge moves out of the near swath at $\Delta t = \tau_p$. As a consequence of the above (cf. the argumentation leading to (12) in Section III-B), the transmit times of the Dirac delta pulse such that the beam-center points at the far and near edges of the swath are given by $\Delta t = \tau_w/2$ and $\tau_p - \tau_w/2$, respectively.

Fig. 4 shows the slant range $r_0(t)$ versus the echo arrival time as determined from (19). The shaded region marks the time duration during which a point at arbitrary range $r_0(t)$ is within the antenna patterns main beamwidth and is equal to the dwell time τ_w. The total echo duration T_{echo} is the difference between the time of the last and first return, as detailed in Section IV-B.

When operating beyond pulse reversal, the far-range echo arrives first, i.e., $t_{\mathrm{far}} < t_{\mathrm{near}}$ as shown in Fig. 4(a) for $O_p = 1.14$. At the reversal point, $O_p = 1$, both near- and far-range echoes arrive at the same time instance, as shown in Fig. 4(b). It is interesting that the minimum echo arrival time is smaller than t_{far} and t_{near} by an amount denoted as the residual time, $\tau_{\mathrm{res}} \geq 0$. Thus, it should be considered that although each range is illuminated by a constant dwell time and $t_{\mathrm{near}} = t_{\mathrm{far}}$, the resulting echo duration is larger than τ_w (as detailed in Section IV-B). In the third case, shown in Fig. 4(c), the f-STEC system operates slightly below the reversal point at $O_p = 0.95$. As mentioned before, the echo compression still occurs, although $t_{\mathrm{near}} < t_{\mathrm{far}}$. Furthermore, note the earliest arrival time is slightly smaller than t_{near} by the residual time τ_{res}.

To compare, Fig. 5 shows the range–time diagram for a conventional stripmap SAR exhibiting a linear range–time dependence and the near-range echo arriving well before the far-range echo.

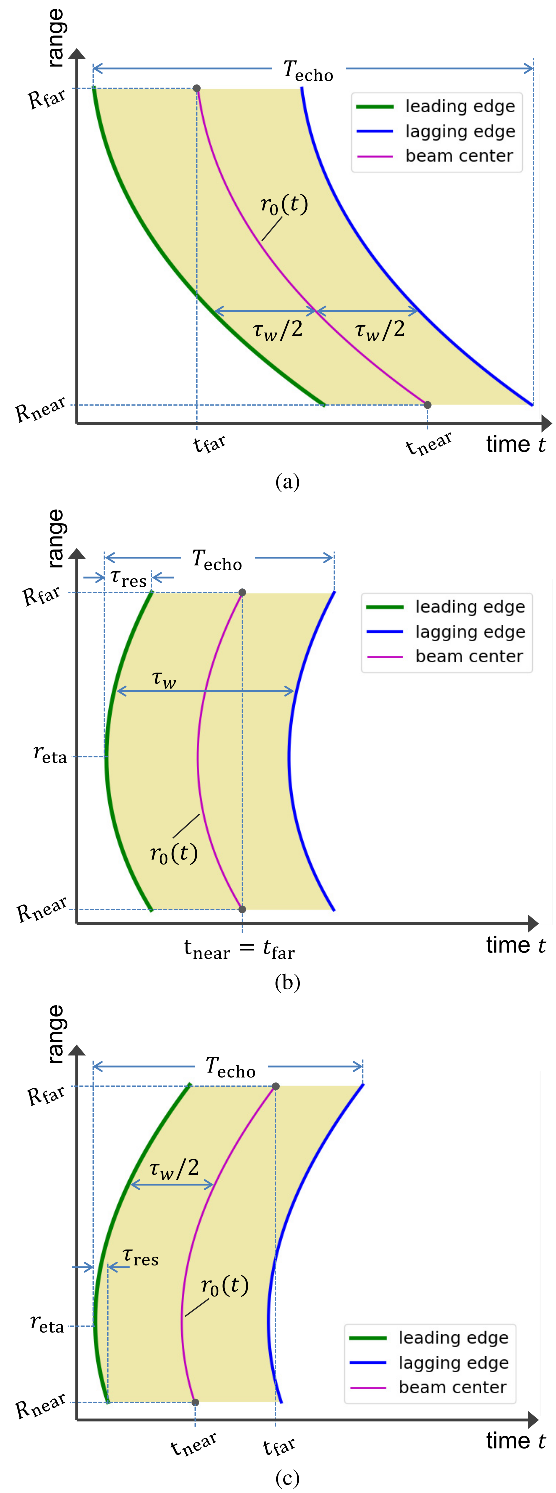

Fig. 4. Range versus time-of-echo arrival for an SAR operating in the f-STEC mode at different operation points. All plots are at the same scale. (a) Operation above the reversal point, $O_p = 1.14$. (b) Operation at the reversal point, $O_p = 1.0$. (c) Operation below the reversal point, $O_p = 0.95$.

B. Echo Window Length

The duration of the echo (typically referred to as echo window length or echo window time) is the time during which the scattered echo signal from the imaged swath arrives at the radar. It is given by

$$T_{\mathrm{echo}} = \left|t_{\mathrm{near}} - t_{\mathrm{far}}\right| + \tau_w + \tau_{\mathrm{res}} \tag{20}$$

where t_{far} and t_{near}, introduced earlier, mark the echo return times at which the beam center moves into and out of the swath, respectively, with the modulus $|\cdot|$ ensuring validity for $t_{\mathrm{far}} \lesseqgtr t_{\mathrm{near}}$; the dwell time τ_w, defined in (8), is added to account for the illumination time of a point scatterer, while the last term is the residual time, which is introduced to consider that the earliest echo return may arrive before, i.e., earlier than, any of the far or near-range echo returns.

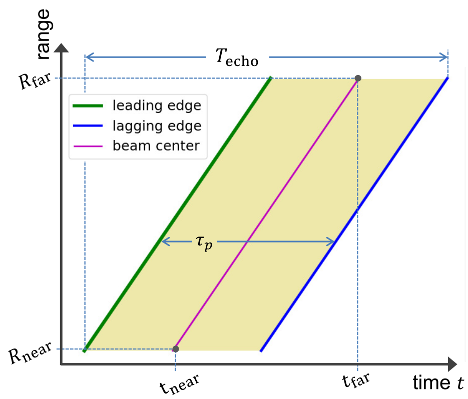

Fig. 5. Range versus time-of-echo arrival for conventional stripmap SAR imaging the same swath width as the f-STEC system. The horizontal scale is extended compared to that in Fig. 4.

Inserting (13) and (14) into the above expressions and rearranging terms give

$$T_{\text{echo}} = \left|\tau_p - \frac{2(R_{\text{far}} - R_{\text{near}})}{c_0} - \tau_w\right| + \tau_w + \tau_{\text{res}}$$
$$= \left(\left|\left(O_p - 1\right)\left(\gamma_w - 1\right)\right| + \gamma_w O_p\right)\tau_0 + \tau_{\text{res}} \qquad (21)$$

which expresses the echo duration in terms of known operational parameters and the residual time τ_{res}. The latter is detailed next as it may affect the echo window length.

1) Residual Time: To determine τ_{res}, the echo return time in (19) is differentiated with respect to Δt, and thus,[5]

$$\frac{\partial t}{\partial \Delta t} = 1 + \frac{2}{c_0}\frac{\partial r_0(t)}{\partial \Delta t}. \qquad (22)$$

Inserting the beam-center range and steering angle from (18) and (11), respectively, and after some simplification yields

$$\frac{\partial t}{\partial \Delta t} = 1 - \frac{2r_O}{c_0}\left(\frac{r_O\cos\theta(t)}{\sqrt{r_E^2 - (r_O\sin\theta(t))^2}} - 1\right)\sin\theta\frac{\Theta_{\text{sc}}}{\tau_p}. \qquad (23)$$

To obtain the saddle point, the above expression has to be set to zero and solved for angle θ_{eta}, which gives the direction of earliest time of arrival (eta), i.e., the direction from which the earliest return echo arrives. A numerical solution for (23) is easily implemented yielding θ_{eta}. In the Appendix, a closed-form solution is derived through a rotation of the coordinate system and approximating the Earth curvature near the swath center by a local flat geometry; the results are shown to be in very good agreement to the numerical solution.

Once the angle θ_{eta} is known, inserting into (18) and (11) yields the corresponding slant range and time delay Δt_{eta}, respectively. Inserting into (19) yields the earliest (minimum) echo time of arrival t_{eta}. Finally, the residual time τ_{res} is defined as the difference between the smaller of t_{near} and t_{far}, and t_{eta} yielding

$$\tau_{\text{res}} = \min\{t_{\text{near}}, t_{\text{far}}\} - t_{\text{eta}}. \qquad (24)$$

[5]The expression in (22) is not given its full credit as it would go beyond the scope of this article. At this point, we merely mention that solving for a predefined $\partial t/\partial\Delta t$ may, among others, be used to "design" a nonlinear steering rate $\theta_0(t)$ so as to yield a specific desired response, equalize intrinsic frequency-scan properties of the antenna, or improve the SNR at the far range, which may lead to the implementation of an adaptive f-STEC.

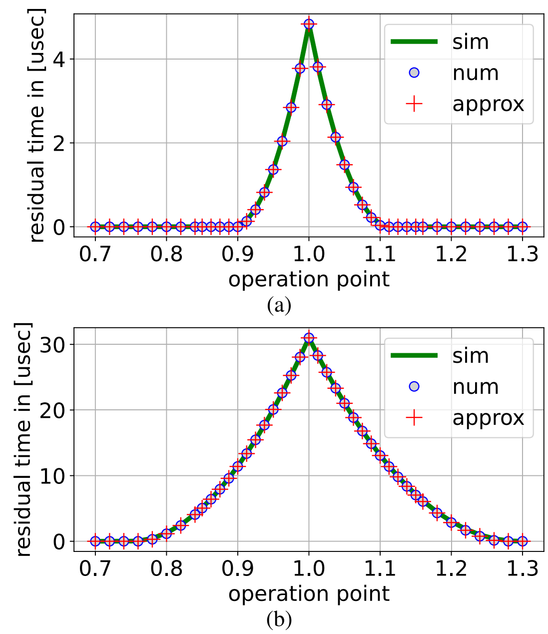

Fig. 6. Residual time versus operation point O_p for two example values of the imaged swath width computed by simulation (green curve), exact numerical approach (circles), i.e., solving (23), and the approximation (plus sign), as in the Appendix. The orbit altitude is 519 km in both cases. (a) Swath width: 50 km and incidence angle: 29°–33.5°. (b) Swath width: 126 km and incidence angle: 29°–39.7°.

The residual time is shown in Fig. 6 plotted versus the operation point for two different configurations imaging a swath of 50 and 126 km. The following is concluded.

1) The maximum residual time is at the reversal point.[6] $O_p = 1$.
2) The value of the maximum residual time (at $O_p = 1$) increases proportionally to the swath width.
3) When $O_p \lessgtr 1$, the residual time falls off (decreases) at a rate inversely proportional to the swath width $R_{\text{far}} - R_{\text{near}}$.
4) The residual time curve is slightly asymmetrical with respect to $O_p = 1$.

With the known residual time, the echo window length is fully determined by (21). Fig. 7 shows T_{echo} versus operation point for a fixed intrinsic duration.[7] At the reversal point, the residual-free echo time (dotted curve in Fig. 7) is at its minimum; this is a general case for f-STEC operation since $0 < \gamma_w < 1$ as can easily be verified from (21). Furthermore, the echo time, i.e., including the residual time, is shown in Fig. 7 to reach its minimum value at the reversal point, where

$$T_{\text{echo}} = \tau_w + \tau_{\text{res}} \quad \text{for} \quad O_p = 1. \qquad (25)$$

C. Pulse Repetition Frequency

A crucial parameter of SAR is the pulse repetition frequency (PRF), which is the reciprocal of the pulse repetition interval (PRI), i.e., $f_{\text{prf}} = 1/T_{\text{pri}}$. It must be ensured (see also later

[6]It can be shown that in this case, the earliest time of arrival is for the echo arriving from mid swath $\theta_{\text{eta}} = (\theta_f - \theta_s)/2$.

[7]Fixing the intrinsic duration τ_0 is equivalent to keeping the swath width constant, in which case varying the operation point O_p implies changing the transmit pulse duration τ_p and, by this, the dwell time $\tau_w = \gamma_w\tau_p$.

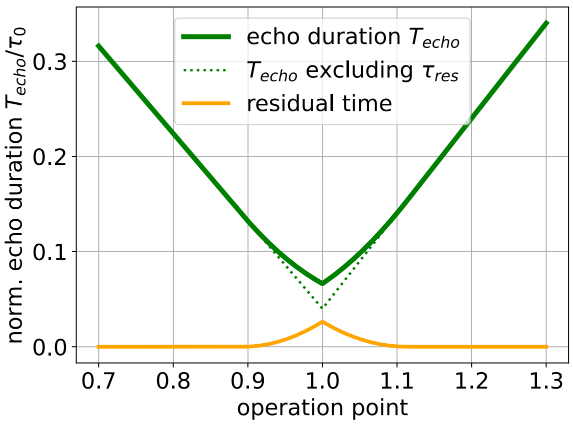

Fig. 7. Echo window length normalized to the intrinsic time versus the operation point. The minimum echo duration is at the reversal point $O_p = 1$.

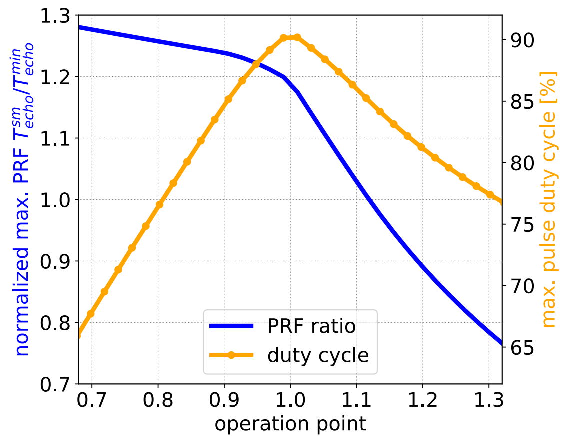

Fig. 8. Maximum PRF of f-STEC SAR relative to the PRF of a stripmap SAR imaging the same swath (left ordinate) and the percentage pulse duty cycle (right ordinate) plotted versus the operation point O_p for an example dwell factor of $\gamma_w = 8\%$. The f-STEC and stripmap parameters are reported in Table I.

discussion in Section IV-D) that the duration of the latter is sufficient to accommodate the transmit pulse duration τ_p and the echo window length T_{echo}, in addition to a margin (guard time) $2\tau_g$ after the fall time and before the rise time of the transmit pulse

$$T_{\text{pri}}^{\min} = T_{\text{echo}} + \tau_p + 2\tau_g. \tag{26}$$

Inserting (21), the minimum PRI may be expressed in terms of the intrinsic echo duration τ_0 and the f-STEC operational parameters as

$$T_{\text{pri}}^{\min} = \begin{cases} 2\tau_p - \tau_0(1-\gamma_w) + \tau_{\text{res}} + 2\tau_g, & O_p > 1 \\ 2\tau_w + \tau_0(1-\gamma_w) + \tau_{\text{res}} + 2\tau_g, & O_p < 1. \end{cases} \tag{27}$$

1) Stripmap SAR PRF and Echo Window Length: It is worth comparing the maximum f-STEC PRF, i.e., minimum PRI, to that of a classical stripmap SAR imaging the same swath width. The stripmap echo window length is given by

$$T_{\text{echo}}^{\text{sm}} = \frac{2}{c_0}(R_{\text{far}} - R_{\text{near}}) + \tau_p^{\text{sm}} \tag{28}$$

where the superscript sm is added to indicate the stripmap operation. Note that the first term in the above expression is proportional to the intrinsic duration τ_0 given in (15). The stripmap PRI is then readily calculated to be

$$\begin{aligned} T_{pri}^{\text{sm}} &= T_{\text{echo}}^{\text{sm}} + \tau_p^{\text{sm}} + 2\tau_g \\ &= \frac{(R_{\text{far}} - R_{\text{near}}) + c_0\tau_g}{c_0(0.5 - \rho^{\text{sm}})} = \frac{\tau_0(1-\gamma_w) + 2\tau_g}{1 - 2\rho^{\text{sm}}} \end{aligned} \tag{29}$$

where a constant pulse duty cycle ρ^{sm} has been assumed such that $\tau_p^{\text{sm}} = \rho^{\text{sm}} T_{pri}^{\text{sm}}$.

The left ordinate in Fig. 8 shows the maximum PRF normalized to the stripmap SAR PRF, $f_{\text{prf}}/f_{\text{prf}}^{\text{sm}}$, versus the operation point, $O_p = \tau_p/\tau_0$. The reversal point is for $\tau_p = \tau_0$, and thus, the system operates in echo time reversal for $O_p > 1$, i.e., abscissa values larger than 1. For the chosen parameter values, the PRF is higher compared to the stripmap case for $O_p \lessapprox 1.12$; this allows a more square-like antenna shape and a better azimuth resolution.

2) Pulse Duty Cycle: A further quantity of interest is the pulse duty cycle, which is the percentage of time the system is transmitting. The expression for the maximum possible duty cycle is obtained from (27) through

$$\rho^{\max} = \frac{\tau_p}{T_{\text{pri}}^{\min}} \tag{30}$$

which is plotted in Fig. 8 (right ordinate). The peak of the duty cycle is at the time reversal point and exhibits exceptionally high values in the order of 90%, much higher (about 5–10 times) than what is usually possible for spaceborne SAR.[8] The high duty cycle values allow for low peak-to-average transmit power and are believed to be a major advantage of f-STEC operation as it significantly reduces the complexity of the transmitter unit and allows for large average transmit power thus improving the SNR, one of the main challenges of spaceborne Ka-band SAR.

The large duty cycle of f-STEC may be utilized in combination with more advanced imaging techniques such as subpulse operation [33], [34], [35], [36]. Transmitting multiple subpulses to illuminate different subswathes within the period of one PRI becomes feasible. This multibeam f-STEC imaging technique, advantageous also for lower frequency SAR, can be used to increase the imaged swath width. Note that introducing subpulses in a conventional operation mode will reduce the available echo window length and, by this, limit the imaged swath width.

It turns out by varying the instrument parameters, e.g., the dwell time has a minor influence on the performance values shown in Fig. 8. It is mainly the operation points O_p and $\Theta_{\text{sw}}/\Theta_{\text{el}}$ that determine the SAR performance. In terms of trade space, this offers the knowledgeable instrument engineer the flexibility to choose the optimum parameters.

D. Swath Position Limits

It was shown that SAR utilizing the f-STEC technique may operate at an extremely high pulse duty cycle while imaging a

[8]FMCW radar, commonly utilized for airborne SAR, operates at 100% duty cycle, but such systems have not been used in space due to the stringent requirement on the transmit–receive antenna decoupling.

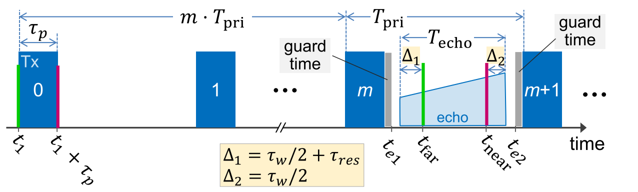

Fig. 9. Timing and echo window position for the case of echo reversal, $O_p > 1$.

wider swath than what would be possible with a conventional stripmap operation mode of the same duty cycle. This, however, does not answer the question as to where the swath is positioned within the possible access range. Conventionally, the imaged swath width and position are determined from the timing (diamond) diagram so as to avoid an overlap of the signal echo and the transmit pulse (cf. [39] for details on the imaging gap caused by the transmit pulses). It turns out that the identical approach is not applicable to f-STEC SAR because of the inherent interrelation between the swath width and various operational parameters. This manifests itself in (21), which shows that the echo duration T_{echo}, the swath width $\propto (R_{\text{far}} - R_{\text{near}})$, and the transmit pulse duration τ_p are not independent parameters.

Nevertheless, a graphical representation similar to the (well known) timing diagram can be obtained, if the f-STEC operation point defined in (16) by $O_p = \tau_p/\tau_0$ is known. This allows the system engineer to start with the required swath width and later determine the (start/stop) position of the swath from the timing diagram.

1) Transmit Pulse Blockage: The approach is to formulate the constraint for the allowable echo time limits within the mth PRI period, where m is an integer that depends on the number of traveling pulses. The time constraint is then used to obtain the slant range limits, which, assuming spherical Earth, has a one-to-one correspondence to the look (off-nadir) and incidence angle.

With reference to Fig. 9, the limits are set such that the receive echo does not coincide with the transmit instances. This yields the mth minimum and maximum allowable echo times

$$t_{e1} = t_1 + mT_{\text{pri}} + \tau_p' \tag{31}$$
$$t_{e2} = t_1 + (m+1)T_{\text{pri}} - \tau_g \tag{32}$$

where τ_g, introduced earlier, is the applicable guard time before and after any transmit pulse, whereas $\tau_p' = \tau_p + \tau_g$ incorporates both the pulse duration as well as the guard time.

Since the two quantities of interest are the (discrete) swath limits, a closed expression may be derived by considering, again, the leading and lagging transmit pulse edges intersecting the reference sphere at times t_1 and $t_1 + \tau_p$ while steered toward the far and near range, respectively. Referring to Fig. 4, the conditions for t_{near} and t_{far} to avoid an overlap of the echo signal with the transmit pulse are readily expressed as

$$\min\{t_{\text{near}}, t_{\text{far}}\} - \tau_{\text{res}} - \frac{\tau_w}{2} \geq t_{e1} \tag{33}$$
$$\max\{t_{\text{near}}, t_{\text{far}}\} + \frac{\tau_w}{2} \leq t_{e2} \tag{34}$$

where the shift by $\pm\tau_w/2$ accounts for t_{near} and t_{far} being relative to the beam center, thus transforming the conditions to be with respect to the earliest/latest echo arrival time.

Consider first the case of echo pulse reversal where $O_p > 1$ and the far-range echo arrives first, and thus, $t_{\text{far}} < t_{\text{near}}$. Inserting (31) into (33) with $\min\{t_{\text{near}}, t_{\text{far}}\} = t_{\text{far}}$ and substituting for t_{far} as in (13) yield

$$\frac{2R_{\text{far}}}{c_0} \geq mT_{\text{pri}} + \tau_p' + \tau_{\text{res}} \tag{35}$$

which is formulated with respect to near range and dwell factor using (9) and (15) to yield the minimum allowable near range in (36).

Furthermore, to avoid an overlap of the echo with the $(m+1)$th transmit pulse, the condition in (34) is applied; thus, inserting (31) and (14) and rearranging as before yield the maximum allowable far range

$$O_p \geq 1 \quad \text{(with echo reversal)}$$
$$\frac{2R_{\text{near}}}{c_0} \geq mT_{\text{pri}} + \tau_p' - (1-\gamma_w)\tau_0 + \tau_{\text{res}} \tag{36}$$
$$\frac{2R_{\text{far}}}{c_0} \leq (m+1)T_{\text{pri}} - \tau_p' + (1-\gamma_w)\tau_0. \tag{37}$$

Following the identical procedure yields the expressions for the limits in terms of the slant range when $O_p < 1$ as:

$$O_p \leq 1 \quad \text{(without echo reversal)}$$
$$\frac{2R_{\text{near}}}{c_0} \geq mT_{\text{pri}} + \tau_w + \tau_g + \tau_{\text{res}} \tag{38}$$
$$\frac{2R_{\text{far}}}{c_0} \leq (m+1)T_{\text{pri}} - \tau_w - \tau_g. \tag{39}$$

The above conditions (alternatively expressed in terms of the look or incidence angle [40], [41]) are valuable for indicating the flexibility, i.e., margin, for placing the imaged swath within the access range. The look angle swath limits are shown in Fig. 10 plotted versus the operation point. Here, $O_p = 0.95$ (indicated by the vertical line) and the PRI is slightly higher than the minimum allowable value given by (27). The blue shaded areas between the minimum near range and maximum far-range swath limits violate the timing conditions; the yellow shaded area marks a 50-km swath. Clearly, from the swath-position point of view, operating the instrument beyond echo reversal provides less flexibility; conversely, a PRI value higher than the minimum $T_{\text{pri}}^{\min}$ allows for variable swath positions.

2) Nadir Echo: The nadir echo signal is caused by near-specular reflection of high amplitude that may saturate the receiver if not sufficiently attenuated by the (two-way) antenna pattern. The nadir return may be mitigated by avoiding the swath ranges blocked by the nadir return through the timing. In the following, closed expressions for the slant ranges masked by the nadir return are derived.

The ground area contributing to the nadir echo is defined by a cone of height h_{sat} and half-angle ϑ_{nd} yielding the minimum and maximum ranges h_{sat} and $l_{nd} = h_{\text{sat}}/\cos\vartheta_{nd}$, respectively (valid for $\vartheta_{nd} \leq 10°$).

Consider the nadir echo of a pulse lasting τ_p seconds transmitted at $t = t_1$. The earliest and latest nadir echo

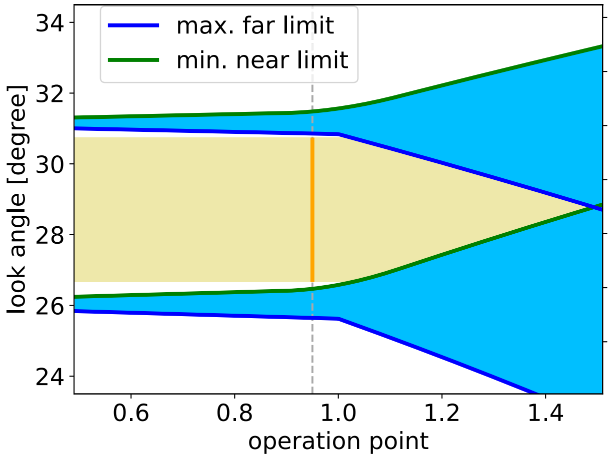

Fig. 10. Near and far swath limits in terms of the look angle plotted versus the operation point. The swath and system parameters are those reported in Table I, specifically here $T_{\text{pri}} = 1.06T_{\text{pri}}^{\min}$ at $O_p = 0.95$. The blue area marks angle ranges blocked by the Tx pulse while the yellow area corresponds to the look angle limits for a 50-km swath.

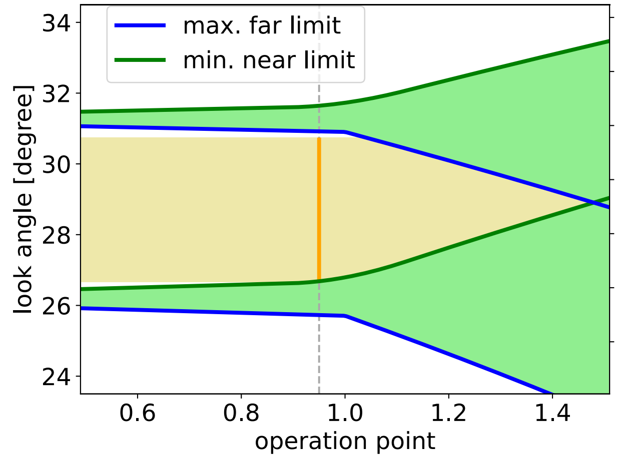

Fig. 11. Near and far swath limits in terms of the look angle plotted versus the operation point. The swath and system parameters are those reported in Table I, specifically here $T_{\text{pri}} = 1.06T_{\text{pri}}^{\min}$ at $O_p = 0.95$. The green area marks the ranges blocked by the nadir return echo, while the yellow area corresponds to the look angle limits for a 50-km swath.

return will arrive, i.e., pass the reference sphere defined earlier, at times $t_1 + 2\ h_{\text{sat}}/c_0$ and $t_1 + \tau_p + 2\ l_{nd}/c_0$, respectively. Clearly, the nadir echo duration

$$T_{nadir} = \tau_p + 2(l_{nd} - h_{\text{sat}})/c_0 \tag{40}$$

is much larger than the SAR echo, cf. (21), as a consequence of $\tau_p > \tau_w$.

To determine the time interval and corresponding slant ranges during which the wanted SAR echo is masked by an unwanted nadir echo, the same approach as for the transmit pulse blockage is followed. The SAR instrument transmits successive pulses at T_{pri} intervals, and the nadir echo return may intervene with the SAR echo of a pulse transmitted $n \cdot T_{\text{pri}}$ seconds earlier. The minimum and maximum allowable SAR echo times are limited by the nadir returns

$$t_{n1} = t_1 + \tau_p + nT_{\text{pri}} + \frac{2l_{nd}}{c_0} \tag{41}$$

$$t_{n2} = t_1 + (n+1)T_{\text{pri}} + \frac{2h_{\text{sat}}}{c_0} \tag{42}$$

and the conditions for t_{near} and t_{far} to avoid an overlap of the echo signal with the nadir return are readily expressed as

$$\min\{t_{\text{near}}, t_{\text{far}}\} - \tau_{\text{res}} - \frac{\tau_w}{2} \geq t_{n1} \tag{43}$$

$$\max\{t_{\text{near}}, t_{\text{far}}\} + \frac{\tau_w}{2} \leq t_{n2}. \tag{44}$$

Proceeding as before yields the swath limits

$$O_p \geq 1 \quad \text{(with echo reversal)}$$

$$\frac{2R_{\text{near}}}{c_0} \geq nT_{\text{pri}} + \frac{2l_{nd}}{c_0} + \tau_p - (1-\gamma_w)\tau_0 + \tau_{\text{res}} \tag{45}$$

$$\frac{2R_{\text{far}}}{c_0} \leq (n+1)T_{\text{pri}} + \frac{2h_{\text{sat}}}{c_0} - \tau_p + (1-\gamma_w)\tau_0 \tag{46}$$

and

$$O_p \leq 1 \quad \text{(without echo reversal)}$$

$$\frac{2R_{\text{near}}}{c_0} \geq nT_{\text{pri}} + \frac{2l_{nd}}{c_0} + \tau_w + \tau_{\text{res}} \tag{47}$$

$$\frac{2R_{\text{far}}}{c_0} \leq (n+1)T_{\text{pri}} + \frac{2h_{\text{sat}}}{c_0} - \tau_w. \tag{48}$$

The expressions above are used to determine the portion of the imaged swath masked, i.e., blocked, by the nadir echo, which, for a given terrain topography, is determined through the respective look angle or slant range interval. The swath limits are plotted in Fig. 11 and are seen to exhibit a nearly identical dependence with respect to the operation point as the transmit pulse blockage (cf. Fig. 10). As such, the same reasoning as before applies to the trade space in terms of swath position and echo reversal operation. Note that placing the swath limits to avoid transmit pulse blockage does not imply a nadir-free echo and vice versa. When positioning the swath, the system engineer needs to take care to independently avoid both nadir return and transmit pulse blockage.

3) Nadir Mitigation Techniques: The constraint imposed by the nadir echo may be relaxed in some cases. For reflector-based SAR, the nadir return may be sufficiently attenuated by the Rx/Tx antenna pattern to avoid contaminating the (wanted) SAR echo. If the nadir return collected by the antenna does not saturate the receiver, then it is sufficient to consider the (shorter) compressed nadir return duration, which relaxes the timing constraint. Furthermore, techniques for the removal of the nadir echo within postprocessing exist, which are based on the alternation of the transmitted waveform [42], [43].

V. SNR Performance

The increased antenna height of an f-STEC SAR system is expected to result in a higher SNR when compared to a conventional stripmap SAR imaging the same swath. Furthermore, it is worth comparing the SNR to that of a digital beamforming system utilizing SCORE. In the following, the SNR expression is derived for these cases giving an insight into the particularities of f-STEC operation mode.

The starting point is the well-known radar equation for extended targets [8], [10] given by

$$\mathrm{SNR} = \frac{P_{\mathrm{av}} A_e^T A_e^R}{4\pi\lambda^2} \frac{\sigma_0}{\mathrm{k}T_N B_{\mathrm{sys}} L_f} \frac{\Phi_{az}}{B_D R(\vartheta)^3 \sin\eta_i} \frac{\chi_\rho}{\tau_p} \times \frac{1}{\Phi_{az}} \int_{\Phi_{az}} |C_{az}(\phi)|^4 \,\mathrm{d}\phi \cdot \frac{1}{\chi_\vartheta} \int_{\chi_\vartheta} |C_{\mathrm{el}}(\vartheta)|^4 \,\mathrm{d}\vartheta \tag{49}$$

where P_{av} is the average transmit power, which is related to the peak power through $P_{\mathrm{av}} = P_t \tau_p f_{\mathrm{prf}} = P_t \rho$; $A_e = \lambda^2 G / 4\pi$ is the effective antenna area written in terms of the antenna gain G [28] where the superscript ^{T} and ^{R} are added to refer to the transmit and receive antenna, respectively; k is Boltzmann's constant; T_N is the system noise temperature; B_{sys} is the bandwidth; L_f is the system loss; χ_ρ and χ_ϑ are the slant range and angular pulse extent, respectively [38]; σ_0 is the backscatter coefficient; B_D is the processed Doppler bandwidth; and Φ_{az} and $C_{az}(\phi)$ are the azimuth beamwidth and normalized radiation pattern, respectively. The last two terms in the above expression represent the azimuth power reduction factor and the two-way pulse extension loss (PEL). The former considers that only the power within the azimuth beamwidth Φ_{az}, which corresponds to the processed Doppler bandwidth, contributes to the SNR as detailed in [8]. The latter considers the loss of the two-way elevation antenna pattern[9] within the angular pulse extent as derived in [38].

A. Stripmap Operation Mode

In the case of the stripmap SAR, the slant range pulse extent is $\chi_\rho = c_0 \tau_p / 2$. Furthermore, the PEL is negligible, i.e., the elevation pattern can be assumed constant within the angular pulse extent, which allows approximating the last term in (49) as

$$\frac{1}{\chi_\vartheta} \int_{\chi_\vartheta} |C_{\mathrm{el}}(\vartheta)|^4 \,\mathrm{d}\vartheta \approx |C_{\mathrm{el}}(\vartheta)|^4 \tag{50}$$

such that the SNR expression becomes

$$\mathrm{SNR}_{\mathrm{sm}} = \frac{P_{\mathrm{av}} (A_e)^2}{8\pi\lambda^2} \frac{\sigma_0 c_0}{\mathrm{k}T_N B_{\mathrm{sys}} L_f} \frac{\Phi_{az}}{B_D R(\vartheta)^3 \sin\eta_i} \times \frac{1}{\Phi_{az}} \int_{\Phi_{az}} |C_{az}(\phi)|^4 \,\mathrm{d}\phi \cdot |C_{\mathrm{el}}(\vartheta)|^4 \tag{51}$$

where $A_e = A_e^T = A_e^R$, i.e., identical antennas for transmission and reception are assumed.

B. Score Operation Mode

For a system operating in SCORE mode, the SNR improves due to the increased receive antenna height $A_R > A_T$. Furthermore, the SNR loss at the swath edges is reduced with respect to the stripmap mode. This gives

$$\mathrm{SNR}_{\mathrm{score}} = \frac{P_{\mathrm{av}} A_e^T A_e^R}{8\pi\lambda^2} \frac{\sigma_0 c_0}{\mathrm{k}T_N B_{\mathrm{sys}} L_f} \frac{\Phi_{az}}{B_D R(\vartheta)^3 \sin\eta_i} \times \frac{1}{\Phi_{az}} \int_{\Phi_{az}} |C_{az}(\phi)|^4 \,\mathrm{d}\phi \cdot \left|C_{\mathrm{el}}^T(\vartheta)\right|^2 \times \frac{1}{\chi_\vartheta} \int_{\chi_\vartheta} |C_{\mathrm{el}}^R(\vartheta)|^2 \,\mathrm{d}\vartheta \tag{52}$$

where the last term represents the one-way PEL of SCORE accounted for by the square of the elevation pattern [38].

C. f-STEC Operation Mode

To arrive at the SNR expression for the f-STEC case, the particularities of this operation mode have to be considered. Remembering that any target "sees" the elevation beamwidth during the dwell time suggests an equivalent slant range pulse extent of $\chi_\rho = c_0 \tau_w / 2$. This effect is not insignificant and reduces (worsens) the SNR by a factor τ_p / τ_w in comparison to the stripmap case. On the other hand, the f-STEC technique allows increasing the transmit and receive antenna height by a factor $\tau_p / \tau_w - 1$, see Section III-A and (8), which improves the SNR by a factor $\approx (\tau_p / \tau_w)^2$ and (over) compensates the earlier effect. However, the two-way PEL also has to be considered for f-STEC, whereas SCORE is only affected by a one-way PEL. Assuming that the pulse power within the elevation beamwidth Θ_{el} is processed, i.e., each target "sees" the elevation beamwidth, allows the following approximation for the integral limits:

$$\frac{1}{\chi_\vartheta} \int_{\chi_\vartheta} |C_{\mathrm{el}}(\vartheta)|^4 \,\mathrm{d}\vartheta \approx \frac{1}{\Theta_{\mathrm{el}}} \int_{\Theta_{\mathrm{el}}} |C_{\mathrm{el}}(\vartheta)|^4 \,\mathrm{d}\vartheta. \tag{53}$$

Then, the expression for the f-STEC SNR becomes

$$\mathrm{SNR} = \frac{P_{\mathrm{av}} (A_e)^2}{8\pi\lambda^2} \frac{\sigma_0 c_0}{\mathrm{k}T_N B_w L_f} \frac{\Phi_{az}}{B_D R(\vartheta)^3 \sin\eta_i} \frac{\tau_w}{\tau_p} \times \frac{1}{\Phi_{az}} \int_{\Phi_{az}} |C_{az}(\phi)|^4 \,\mathrm{d}\phi \cdot \frac{1}{\Theta_{\mathrm{el}}} \int_{\Theta_{\mathrm{el}}} |C_{\mathrm{el}}(\vartheta)|^4 \,\mathrm{d}\vartheta \tag{54}$$

where the noise contribution within the processed resolution bandwidth B_w is considered, which works in favor of improving the SNR with respect to stripmap since $B_w < B_{\mathrm{sys}}$.

VI. Instrument Performance Comparison

In this section, we compare the performance of a Ka-band SAR instrument operating in the f-STEC mode to a conventional SAR operating in the stripmap mode and to a, more advanced, digital beamforming SAR utilizing SCORE. The three instruments are designed to image a 50-km swath, the average transmit power is assumed to be 100 W, and the spatial 2-D image resolution is to be 7.4 m^2.

The resulting instruments and operation parameters are listed in Table I. The values of some of the common parameters, e.g., system noise temperature and losses, do not take the instrument hardware differences into account and may be considered optimistic. However, these have no impact on the relative performance comparison between the systems, which is the purpose here.

[9] In [38], only the effect of the receive, i.e., one-way antenna pattern within the angular pulse extent, is considered, as applicable for a DBF system utilizing SCORE. For f-STEC, the expression is modified to consider both the receive and transmit antenna patterns resulting in a $|C_{\mathrm{el}}(\vartheta)|^4$ dependence.

TABLE I

SYSTEM AND INSTRUMENT PARAMETERS FOR THE THREE SAR SYSTEMS COMPARED IN TERMS OF NOISE-EQUIVALENT SIGMA-ZERO PERFORMANCE

parameter	f-STEC	Stripmap	SCORE
orbit height , h_{sat}	$519\,\text{km}$		
wavelength , λ	$8.3\,\text{mm}$		
swath width	$50\,\text{km}$		
incidence angle , η_i	$29°$ to $33.5°$		
average power , P_{av}	$100\,\text{W}$		
antenna beamwidth factor , γ_{el}	0.89		
noise temperature / losses , T_N / L_f	$300\,\text{K}$ / $3\,\text{dB}$		
pulse repetition frequency , f_{prf}	$4625\,\text{Hz}$	$3875\,\text{Hz}$	
pulse duty cycle , ρ	$82.8\,\%$	$15\,\%$	
chirp bandwidth , B_{sys}	$500\,\text{MHz}$	$48\,\text{MHz}$	
processed Doppler , B_D	$3.85\,\text{kHz}$	$3.23\,\text{kHz}$	
data rate , D_r	$112\,\text{MS/s}$	$78\,\text{MS/s}$	
antenna area (Tx/Rx)	$3.5\,\text{m}^2$	$0.35\,\text{m}^2$	$0.35\,\text{m}^2$ / $2.5\,\text{m}^2$
aspect ratio (Tx/Rx)	2.4	35	35 / 4.7
pulse extension loss , PEL	$1.6\,\text{dB}$	-	$2\,\text{dB}$
swath-to-beamwidth ratio , Θ_{sw}/Θ_{el}	11.5 (Tx,Rx)	1 (Tx,Rx)	1 (Tx) , 7 (Rx)
azimuth loss	$1.2\,\text{dB}$	$1.2\,\text{dB}$	
range/azimuth resolution	$3.7\,\text{m}$ / $2\,\text{m}$	$3.1\,\text{m}$ / $2.4\,\text{m}$	
dwell factor , γ_w	0.08	-	
operation point , O_p	0.95	-	

A. Swath Timing and PRF

The timing diagram of the f-STEC system shown in Fig. 12(a) is computed based on the equations derived in Section IV-D; it appears similar to the well-known diamond diagram but for an instrument operating at a low pulse duty cycle, whereas f-STEC benefits from the return echo compression and operates at a high duty cycle of 82%. To compare, the timing diagram common for the stripmap and SCORE instrument modes is shown in Fig. 12(b); the transmit blockage appears much wider although the pulse duty cycle is only 15%. The imaged swath off-nadir angular position is chosen to be the same as for the f-STEC systems; the swath is shown to be intersected by nadir returns, which is allowed (assuming that it can be suppressed [42]) in favor of a better comparison between the different instruments.

B. Spatial Resolution

The instruments and mode parameters are designed to yield the same 2-D resolution of 7.4 m^2 for all systems. Since (for nonsquinted SAR) the 2-D resolution is the product of range and azimuth resolution [44], it affects the processed range (chirp) and Doppler bandwidths. The latter is directly determined by the PRF assuming an 120% azimuth oversampling. For the f-STEC system, the range resolution results from the dwell factor and the system bandwidth, while the chirp bandwidth of the stripmap and SCORE systems is chosen to yield the required 2-D resolution.

C. Antenna Sizes

The Tx/Rx antenna size of the f-STEC system results from following the design procedures elaborated in the previous sections. Thus, the dwell factor together with the available chirp bandwidth determines the beamwidth and, by this, the antenna height. The antenna length mainly results from the timing diagram, i.e., the PRF suitable for imaging the required swath width.

The stripmap instrument antenna height is determined from (1) so as to illuminate the complete swath width. The antenna length is determined by the PRF, which is lower compared to the f-STEC case resulting in a longer antenna for the stripmap system.

The transmit antenna of the SCORE system is identical to that of the stripmap instrument and the same is true for the Rx antenna length. Theoretically, the height of the Rx antenna may be of an arbitrarily high value; practically, it is limited by the complexity since increasing the antenna height requires more digital channels to implement SCORE and at some point also requires dispersive onboard beamforming to mitigate the PEL [38], [45]. Here, the antenna height was chosen so as to limit the PEL to about 2.5 dB.

D. Data Rate

The data rate is a relevant system parameter as it determines the required onboard memory and downlink capacity of the satellite. The data rate in sample per second, i.e., independent analog-to-digital (ADC) converter resolution, is computed

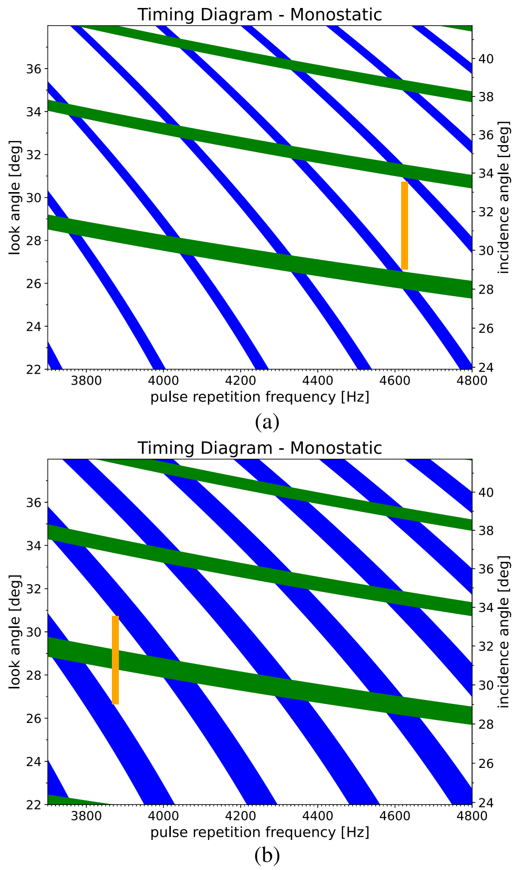

Fig. 12. Timing (diamond) diagram showing the blockage due to the transmit instances (blue strips) and the nadir echo return (green strips) versus PRF. The angular position of the imaged swath is indicated by the orange bar. (a) f-STEC. (b) Stripmap and SCORE.

according to:

$$D_r = \frac{2\gamma_s B_{\text{sys}} T_{\text{echo}}}{T_{\text{pri}}} \tag{55}$$

where $\gamma_s B_{\text{sys}}$ is the ADC sampling frequency and γ_s is the oversampling factor.

The reported values in Table I indicate a 43% higher data rate for the f-STEC instrument compared to the other systems, although all systems image an identical swath width with equal 2-D resolution. This is attributed to two main effects.

1) The finer azimuth resolution requires an increased azimuth sampling for the f-STEC system of $T_{\text{pri}}^{\text{sm}}/T_{\text{pri}}$, where the superscript sm indicates the stripmap parameter. With the values of Table I, this increases the data rate by a factor ≈ 1.2.
2) With $O_p = 0.95$, the instrument is operating slightly below the reversal point, the increased echo duration causes a proportionally higher data rate, which is not "compensated" by the lower system bandwidth. The relative contribution of this effect is $B_{\text{sys}} T_{\text{echo}}/(B_{\text{sys}}^{\text{sm}} T_{\text{echo}}^{\text{sm}})$ amounting to an increased data rate by a similar factor ≈ 1.2.

The effect of the latter point can be compensated since the instantaneous bandwidth of the received echo is smaller than B_{sys}; this reduction becomes significant when $O_p \lessapprox 1$ and offers the opportunity for onboard data rate reduction as discussed in [25], [46], and [47]. However, we maintain that this type of data reduction merely compensates for the aforementioned increased echo window length.

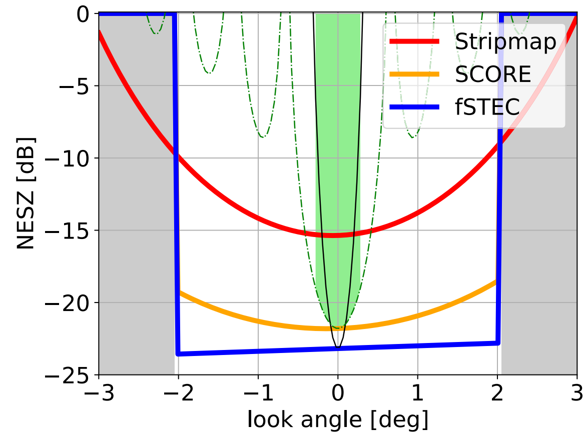

Fig. 13. NESZ comparison of the stripmap, SCORE, and f-STEC systems. The two-way stripmap antenna pattern follows the shape of the respective NESZ curve, while black dashed and solid curves represent the Rx SCORE and f-STEC patterns, respectively.

E. Noise-Equivalent Sigma Zero

The three systems are compared with respect to their noise-equivalent sigma zero (NESZ), calculated according to NESZ $= \sigma_0|_{\text{SNR}=1}$ [8], [9]. Fig. 13 shows the NESZ versus the swath-centered look angle. The f-STEC system is characterized by a nearly constant NESZ over the swath, which is due to the Tx/Rx beam scanning property. Note that the loss associated with the short point target pulse duration, cf. factor τ_w/τ_p in (54), degrades the NESZ by a factor of 11 dB with respect to stripmap and SCORE for the parameters given in Table I.

Nevertheless, f-STEC clearly outperforms the stripmap system, the main reason being the small antenna area of the latter, which further suffers from an extremely high length-to-height aspect ratio of 35 (cf. Table I).

The SCORE system shows a reasonably good performance nearly reaching that of f-STEC at the swath center. Despite its good performance, the SCORE system can be considered an inferior choice at higher carrier frequencies (Ka-band and above) because of its high complexity and technology demand (multichannel RF hardware and onboard digital processing unit) [3], [15], [16], [17], [18].

The roll-off at the swath borders of the stripmap and SCORE SAR systems is due to the fixed low-gain transmit pattern. This well-known effect occurs mainly for planar phased direct radiating antennas and can be mitigated by increasing the antenna height and introducing dedicated phase tapering techniques [48], [49] known as phase spoiling. This will flatten the radiation pattern shape, thus improving the performance near the swath edges at the expense of degradation near the swath center.

Last but not least, it is noted that assuming the same average transmit power $P_{\text{av}} = 100\,\text{W}$ for all three systems penalizes f-STEC since it does not benefit from the high pulse duty cycle of 82%. Stated differently, the peak-to-average power ratio of the stripmap/SCORE instruments is 5.5 times higher than that of the f-STEC instrument.

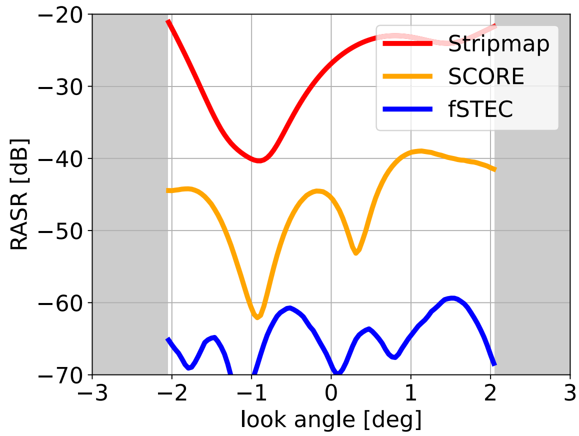

Fig. 14. RASR comparison of the stripmap, SCORE, and f-STEC systems.

F. Azimuth and Range Ambiguities

The azimuth-ambiguity-to-signal ratio is approximately the same for all three systems, given that the processed Doppler oversampling was fixed to 120%.

The range-ambiguity-to-signal ratio (RASR) estimation [50] is shown in Fig. 14. The best performance is for the f-STEC system followed by the SCORE instrument and with the stripmap system having the poorest performance. This is attributed to the respective two-way elevation pattern beamwidths. However, in general, the ambiguity level is low for all three systems since the performance is timing-limited. Nevertheless, both SCORE and f-STEC systems could be operated in a multiswath imaging mode [39], without sacrificing RASR.

VII. Conclusion

This underlying article provides an in-depth insight into the f-STEC imaging technique and its utilization for SAR. This article derived the essential mode and instrument parameters necessary for a thorough understanding of the f-STEC technique. With this, two main purposes were served: 1) simple analytic formulas were provided and analyzed in detail to allow for the design of an f-STEC instrument and 2) the equations governing the performance of an f-STEC system were derived and used to provide a comparison between three SAR systems utilizing in different categories of imaging modes. The reported performances suggest that f-STEC may be an especially advantageous choice for SAR systems operating at higher carrier frequencies such as X-band, Ka-band, and above. In fact, given the current technology readiness level of space-qualified Ka-band components, f-STEC might be considered the only feasible choice.

This article revisits an imaging technique, which in its general form has been referred to as f-Scan [21], [22], [23], [24]. The new contributions of this article, which introduces a particular realization of f-Scan, can be summarized as follows.

1) The entire set of analytic equations describing the f-STEC imaging mode parameters is derived from the basic principles.
2) The echo window timing and blockage types are treated in detail deriving the governing mathematical expressions. This enables the system engineer to design the timing for a specific swath width and position instead of relying on simulations.
3) Closed-form expressions for the SNR performance and data rate are provided allowing a straightforward comparison to other imaging modes.

An aspect worth further investigation is the utilization of nonlinear time-to-angle steering or time–frequency chirps. For example, it is straightforward to change the steering law to obtain a constant ground range resolution over the swath (corresponding to a variable slant range resolution). The theoretical groundwork has been established in this article but used (only) to derive the expressions for the residual time in Section IV-B. We recognize a high potential of utilizing (22) to fine-tune the system and further improve the performance or, even more, for an adaptive f-STEC SAR adjusting the scan rate to image interesting swath portions at finer resolution and higher SNR. This adaptive approach may conveniently be combined with multibeam f-STEC technique, c.f. Section IV-C2, to image multiple subswathes at different resolutions.

Two topics have not been covered since they are addressed in previous publications and would exceed the scope of this article: the realization and technology for frequency-scanning antennas [21], [22], and processing of f-STEC data to yield the SAR image [24]. Both are considered important and are subject to further research intended for future publications.

Appendix
Local Flat Earth Geometry Approximation

For a moderate swath width, a good approximation of the slant range can be made assuming local flat Earth geometry at the swath center. As shown in Fig. 15, the satellite coordinates are rotated by the angle by β_c with respect to nadir to form the right angle triangle from the slant range at swath center R_c, the tangential to the Earth surface, and the modified satellite height $\hat{h}_{\text{sat}}$. The unknown parameters are determined from the geometry shown in the figure to be

$$\beta_c = \eta_{ic} - \theta_{0c} \tag{56}$$
$$\hat{h}_{\text{sat}} = R_c \cos(\theta_{0c} + \beta_c) \tag{57}$$

where η_{ic} and $\theta_{0c} = (\theta_{\text{near}} + \theta_{\text{far}})/2$ are the local incidence and look (off nadir) angles at swath center, respectively.

The equation for the approximate slant range $\tilde{r}_0(t)$ as a function of beam-center look angle $\theta_0(t)$ then becomes

$$\tilde{r}_0(t) = \frac{\hat{h}_{\text{sat}}}{\cos\hat{\theta}_0(t)} \quad \text{with} \quad \hat{\theta}_0(t) = \beta_c + \theta_0(t). \tag{58}$$

Inserting into (19), differentiating with respect to Δt, and setting the result equal to zero give

$$\frac{\partial \tilde{t}}{\partial \Delta t} = 1 + \frac{2}{c_0}\frac{\partial \tilde{r}_0(t)}{\partial \Delta t} \stackrel{!}{=} 0$$
$$\Rightarrow 1 - \frac{2\hat{h}_{\text{sat}}\Theta_{\text{sc}}}{c_0 \tau_p} \tan\hat{\theta}_0(t) \sec\hat{\theta}_0(t) \stackrel{!}{=} 0. \tag{59}$$

Rearranging and formulating the result in terms of angle $\hat{\theta}_{\text{eta}} = \beta_c + \theta_{\text{eta}} = \beta_c + \theta(t_{\text{eta}})$, i.e., the angle at which the main beam is pointing to the direction of minimum echo

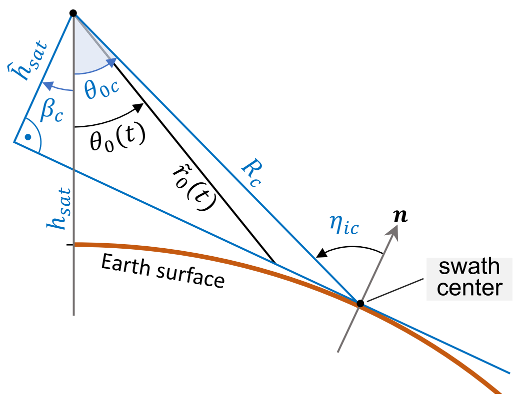

Fig. 15. Equivalent geometry for local flat Earth approximation.

time of arrival, the operation point yields the following closed expression:

$$\tan\hat{\theta}_{\text{eta}}\sec\hat{\theta}_{\text{eta}} = \frac{(R_{\text{far}} - R_{\text{near}}) \cdot O_p}{\hat{h}_{\text{sat}}\Theta_{\text{sw}}}. \tag{60}$$

For a not-too-wide swath, the angular extent of $\theta_0(t)$ is limited and the left-hand side of (60) can be approximated by a straight line, finally yielding

$$\theta_{\text{eta}} \approx \frac{1}{B}\frac{(R_{\text{far}} - R_{\text{near}}) \cdot O_p}{\hat{h}_{\text{sat}}\Theta_{\text{sw}}} - \beta_c \tag{61}$$

where the slope B is

$$\begin{aligned} B &= \frac{\partial}{\partial\Delta t}\tan\hat{\theta}_0(t)\sec\hat{\theta}_0(t)\Big|_{\hat{\theta}_0(t)=\beta_c+\theta_{0c}} \\ &= \sec(\beta_c+\theta_{0c})\left(\tan^2(\beta_c+\theta_{0c}) + \sec^2(\beta_c+\theta_{0c})\right). \end{aligned} \tag{62}$$

References

[1] I. Hajnsek, "The Ka-band interferometric radar mission proposal for cold environments-SKADI," in *Proc. Adv. RF Sensors Remote Sensing Instrum. (ARSI)*, May 2022.

[2] C. Schaefer, M. Volker, P. Lopez-Dekker, M. Younis, E. Daganzo-Eusebio, and M. Ludwig, "Space-borne Ka-band across-track SAR interferometer," in *Proc. 1st Workshop Ka-Band Earth Observ. Radar Missions (KEO)*. Noordwijk, The Netherlands: ESA-ESTEC, Nov. 2012, pp. 1–8.

[3] P. Lopez-Dekker, M. Younis, J. A. Garcia, T. Borner, and G. Krieger, "Advanced digital beamforming architectures and operation modes for an enhanced SIGNAL mission concepts," in *Proc. 1st Workshop Ka-Band Earth Observ. Radar Missions (KEO)*, Noordwijk, The Netherlands, Nov. 2012, pp. 1–8.

[4] D. Moller et al., "The glacier and land ice surface topography interferometer: An airborne proof-of-concept demonstration of high-precision Ka-band single-pass elevation mapping," *IEEE Trans. Geosci. Remote Sens.*, vol. 49, no. 2, pp. 827–842, Feb. 2011.

[5] Catalyst: Strategic New Zealand–German Aerospace Centre Joint Research Programme. (May 2022). *Project Takahe: Advanced Object Detectability in a Water Clutter Environment Using InSAR*. [Online]. Available: https://shorturl.at/uwHY0

[6] A. Freeman et al., "The 'Myth' of the minimum SAR antenna area constraint," *IEEE Trans. Geosci. Remote Sens.*, vol. 38, no. 1, pp. 320–324, Jan. 2000.

[7] M. Younis, P. Lopez-Dekker, F. Bordoni, P. Laskowski, and G. Krieger, "Exploring the trade-space of MIMO SAR," in *Proc. IEEE Int. Geosci. Remote Sens. Symp. (IGARSS)*, Jul. 2013, pp. 4455–4458.

[8] R. K. Raney, "SNR in SAR," in *Proc. Int. Geosci. Remote Sens. Symp. (IGARSS)*, Amherst, MA, USA, Oct. 1985, pp. 994–999.

[9] M. Younis, P. Löpez-Dekker, G. Krieger, and A. Moreira, "Digital beamforming signal-to-noise ratio gain in multi-channel SAR," in *Proc. Int. Geosci. Remote Sens. Symp. (IGARSS)*, Milan, Italy, Jul. 2015, pp. 2778–2781.

[10] M. Younis, "NESZ-formulation for planar multi-channel SAR," German Aerosp. Center, Microw. Radar Inst., Tech. Rep., HR-RK-TN MY101, Apr. 2019.

[11] A. Moreira, P. Prats-Iraola, M. Younis, G. Krieger, and I. P. K. Hajnsek, "A tutorial on synthetic aperture radar," *IEEE Geosci. Remote Sens. Mag.*, vol. 1, no. 1, pp. 6–43, May 2013.

[12] M. Suß and W. Wiesbeck, "Side-looking synthetic aperture radar system," European Patent EP 1 241 487, Sep. 18, 2002.

[13] J. H. Blythe, "Radar systems," U.S. Patent 4 253 098, Feb. 6, 1981.

[14] J. T. Kare, "Moving receive beam method and apparatus for synthetic aperture radar," U.S. Patent 6 175 326, Jan. 1, 2001.

[15] M. Ludwig and S. D'Addio, "Ka-band SAR feasibility study," European Space Agency (ESA), Tech. Rep., TEC-ETP/2009.122.ML, Sep. 2009.

[16] P. Lopez-Dekker et al., "Ka-band SAR application consolidation and requirement definition study," European Space Agency (ESA), Tech. Rep., ESA AO/1-9011/17/NL/FF/gp, Apr. 2020.

[17] M. Younis, P. Lopez-Dekker, A. Patyuchenko, and G. Krieger, "Digital beamforming architecture and techniques for a spaceborne interferometric Ka-band mission," in *Proc. IEEE Radar Conf. (RadarCon)*, Ottawa, ONT, Canada, Apr. 2013, pp. 1–5.

[18] C. Schaefer and P. Lopez-Dekker, "Interferometric Ka-band SAR with DBF capability," in *Proc. Eur. Conf. Synth. Aperture Radar (EUSAR)*, Nuermberg, Germany, May 2012, pp. 7–10.

[19] M. Ettorre, R. Sauleau, L. L. Coq, and F. Bodereau, "Single-folded leaky-wave antennas for automotive radars at 77 GHz," *IEEE Antennas Wireless Propag. Lett.*, vol. 9, pp. 859–862, 2010.

[20] D. A. Schneider, M. Rosch, A. Tessmann, and T. Zwick, "A low-loss W-band frequency-scanning antenna for wideband multichannel radar applications," *IEEE Antennas Wireless Propag. Lett.*, vol. 18, no. 4, pp. 806–810, Apr. 2019.

[21] C. Roemer, "Introduction to a new wide area SAR mode using the F-SCAN principle," in *Proc. IEEE Int. Geosci. Remote Sens. Symp. (IGARSS)*, Jul. 2017, pp. 3844–3847.

[22] C. Römer, R. Gierlich, J. Marquez-Martinez, and M. Notter, "Frequency scanning applied to wide area SAR imaging," in *Proc. Eur. Conf. Synth. Aperture Radar (EUSAR)*, Aachen, Germany, Jun. 2018, pp. 1–5.

[23] C. Römer, "High resolution wide swath synthetic aperture radar system," U.S. Patent 0 174 114, Mar. 12, 1986.

[24] L. Nan, G. Gai, T. Shiyang, and Z. Linrang, "Signal modeling and analysis for elevation frequency scanning HRWS SAR," *IEEE Trans. Geosci. Remote Sens.*, vol. 58, no. 9, pp. 6434–6450, Sep. 2020.

[25] R. Scheiber, M. Martone, and N. Gollin, "Chirp selection and data compression for spaceborne wide-swath SAR in FScan-mode," in *Proc. Eur. Conf. Synth. Aperture Radar (EUSAR)*, Jul. 2021, pp. 1–6.

[26] P. Guccione, D. Mapelli, D. Giudici, and A. R. Persico, "Design of f-SCAN acquisition mode for synthetic aperture radar," *Remote Sens.*, vol. 14, no. 20, p. 5283, 2022. [Online]. Available: https://www.mdpi.com/2072-4292/14/20/5283

[27] C. Fischer, C. Schaefer, and C. Heer, "Technology development for the HRWS (high resolution wide swath) SAR," in *Proc. Int. Radar Symp. (IRS)*, Sep. 2007.

[28] C. A. Balanis, *Antenna Theory: Analysis and Design*, 4th ed. Chichester, NY, USA: Wiley, 2016.

[29] M. Secmen, S. Demir, A. Hizal, and T. Eker, "Frequency diverse array antenna with periodic time modulated pattern in range and angle," in *Proc. IEEE Radar Conf.*, Apr. 2007, pp. 427–430.

[30] W.-Q. Wang, H. C. So, and A. Farina, "An overview on time/frequency modulated array processing," *IEEE J. Sel. Topics Signal Process.*, vol. 11, no. 2, pp. 228–246, Mar. 2017.

[31] C. A. Balanis, *Advanced Engineering Electromagnetics*, 2nd ed. Hoboken, NJ, USA: Wiley, 2012.

[32] M. Younis, S. Huber, A. Patyuchenko, F. Bordoni, and G. Krieger, "Performance comparison of Reflector- and planar-antenna based digital beam-forming SAR," *Int. J. Antennas Propag.*, vol. 2009, pp. 1–13, Jun. 2009. [Online]. Available: http://www.hindawi.com/journals/ijap/2009

[33] M. Younis, F. Bordoni, G. Krieger, P. Löpez-Dekker, and F. D. Zan, "Synthetik-apertur-radarverfahren und synthetik-apertur-radarsystem," German Patent DE 2 21 756, Oct. 13, 2014.

[34] M. Younis, F. Bordoni, G. Krieger, P. Löpez-Dekker, and F. D. Zan, "Synthetik-apertur-radarverfahren und synthetik-apertur-radarsystem," German Patent EP 3 060 939-B1, Nov. 8, 2018.

[35] M. Younis, G. Krieger, and A. Moreira, "MIMO SAR techniques and trades," in *Proc. EuRAD*, Nuremberg, Germany, Oct. 2013, pp. 141–144.

[36] M. Younis, P. Lopez-Dekker, and G. Krieger, "MIMO SAR operation modes and techniques," in *Proc. Eur. Conf. Synth. Aperture Radar (EUSAR)*, Berlin, Germany, Jun. 2014, pp. 1–3.

[37] G. Krieger, N. Gebert, and A. Moreira, "Multidimensional waveform encoding: A new digital beamforming technique for synthetic aperture radar remote sensing," *IEEE Trans. Geosci. Remote Sens.*, vol. 46, no. 1, pp. 31–46, Jan. 2008.

[38] M. Younis, T. Rommel, F. Bordoni, G. Krieger, and A. Moreira, "On the pulse extension loss in digital beamforming SAR," *IEEE Geosci. Remote Sens. Lett.*, vol. 12, no. 7, pp. 1436–1440, Jul. 2015.

[39] M. Younis, F. Q. de Almeida, M. Villano, S. Huber, G. Krieger, and A. Moreira, "Digital beamforming for spaceborne reflector-based synthetic aperture radar. Part 2: Ultra-wide swath imaging mode," *IEEE Geosci. Remote Sens. Mag.*, early access, Oct. 28, 2022, doi: 10.1109/MGRS.2022.3200871.

[40] M. Younis and T. Bollian, "Circular orbit SAR geometry," German Aerosp. Center, Microw. Radar Inst., Tech. Rep., TN-RK-ST-TN7562, Mar. 2022.

[41] R. K. Raney, "Doppler properties of radars in circular orbits," *Int. J. Remote Sens.*, vol. 7, no. 9, pp. 1153–1162, Sep. 1986.

[42] M. Villano, G. Krieger, and A. Moreira, "Nadir echo removal in synthetic aperture radar via waveform diversity and dual-focus postprocessing," *IEEE Geosci. Remote Sens. Lett.*, vol. 15, no. 5, pp. 719–723, May 2018.

[43] S.-Y. Jeon, T. Kraus, U. Steinbrecher, G. Krieger, and M. Villano, "Experimental demonstration of nadir echo removal in SAR using waveform diversity and dual-focus postprocessing," *IEEE Geosci. Remote Sens. Lett.*, vol. 19, pp. 1–5, 2022.

[44] G. P. Cardillo, "On the use of the gradient to determine bistatic SAR resolution," in *Proc. IEEE AP-S Int. Symp.*, May 1990, pp. 1032–1035.

[45] M. Younis, F. Q. de Almeida, M. Villano, S. Huber, G. Krieger, and A. Moreira, "Digital beamforming for spaceborne reflector-based synthetic aperture radar, Part 1: Basic imaging modes," *IEEE Geosci. Remote Sens. Mag.*, vol. 9, no. 3, pp. 8–25, Sep. 2021. [Online]. Available: https://www.nxtbook.com/nxtbooks/ieee/geoscience_september2021

[46] N. Gollin and M. Martone, "Block-frequency quantization for data volume reduction in FS can systems," in *Proc. Eur. Conf. Synth. Aperture Radar (EUSAR)*, Leipzig, Germany, Jul. 2022.

[47] N. Gollin, R. Scheiber, M. Martone, P. Rizzoli, and G. Krieger, "SAR imaging in frequency scan mode: System optimization and potentials for data volume reduction," *IEEE Trans. Geosci. Remote Sens.*, to be published.

[48] R. Kinsey, "Phased array beam spoiling technique," in *Proc. IEEE Int. Symp. Antennas Propag.*, vol. 2, Montreal, QC, Canada, 1997, pp. 698–701.

[49] M. Villano, G. Krieger, and A. Moreira, "Advanced spaceborne SAR systems with planar antenna," in *Proc. IEEE Radar Conf. (RadarConf)*, Seattle, WAS, USA, May 2017, pp. 152–156.

[50] J. C. Curlander and R. N. McDonough, *Synthetic Aperture Radar: Systems and Signal Processing*. Hoboken, NJ, USA: Wiley, 1991.

Marwan Younis (Fellow, IEEE) received the B.Sc. degree in electrical engineering from the University of Baghdad, Iraq, in 1992 and the Dipl.Ing. (M.Sc.) and Dr.Ing. (Ph.D.) degree in electrical engineering from the Universität Karlsruhe (TH), Germany, in 1997 and 2004, respectively.

From 1998 to 2004, he was a Research Scientist with the Institut für Höchstfrequenztechnik und Elektronik, Universität Karlsruhe. Since 2005, he has been with the Microwaves and Radar Institute of the German Aerospace Center (DLR), Oberpfaffenhofen, Germany. He is currently Head of the SAR Techniques Group at the DLR and Professor for Spaceborne Radar Systems at the Karlsruhe Institute for Technology (KIT), Karlsruhe, Germany. He is the author and coauthor of about 200 conference papers, 46 reviewed publications and holds 5 patents. His research fields include synthetic aperture radar (SAR) systems and techniques, MIMO SAR, digital beamforming, SAR performance, calibration, and antennas. In 1996, he was an Intern at the Jet Propulsion Laboratory (JPL), in 2013 and 2019, he spent Research Sabbaticals at JPL.

Dr. Younis is an active member of the IEEE and GRSS. He served GRSS AdCom, from 2018 until 2020. He chaired the Instrumentation and Future Technologies GRSS Technical Committee. He is reviewer of IEEE publications and was an Associate Editor for the IEEE geoscience and remote sensing letter (2012-2019). He received the Hermann-Billing award for his Ph.D. thesis in 2005.

Felipe Queiroz de Almeida received the B.S.E.E. (Hons.) and M.S.E.E. degrees in electronic engineering from the Aeronautics Technological Institute (ITA), São José dos Campos, Brazil, in 2009 and 2011, respectively, and the Dr.Ing. (Ph.D.) degree (Hons.) in electrical engineering from the Karlsruhe Institute of Technology (KIT), Karlsruhe, Germany, in 2018. He developed his bachelor's thesis at Microwaves and Radar Institute, German Aerospace Center (DLR-HR), Weßling, Germany.

In 2009, he was a Research Intern with the Microwaves and Radar Institute, DLR-HR. From 2011 to 2014, he was with Bradar Indústria S.A., São José dos Campos, where he worked on Software Development for synthetic aperture radar applications. Since November 2014, he has been with DLR-HR, first as a Ph.D. Student and then as a Researcher. His research interests include radar signal processing and digital beamforming, in particular beamforming techniques for high-resolution wide-swath synthetic aperture radar (SAR).

Dr. Queiroz de Almeida received the EADS Argus Student Award 2010 for his bachelor's thesis, the Franz-Xaver-Erlacher Award for Young Scientists in 2015, and the ITG Award in 2019 for the best research paper.

Tobias Bollian (Member, IEEE) received the B.Sc., M.Sc., and Ph.D. degrees in electrical engineering from the Karlsruhe Institute of Technology, Karlsruhe, Germany, in 2012, 2014, and 2019, respectively.

In 2013, he was a Student Researcher with the Alaska Satellite Facility, Fairbanks, AK, USA. From 2014 to 2015, he was with the European Space Agency's (ESA's) European Space Research and Technology Center, Noordwijk, The Netherlands, under the Young Graduate Trainee Program. From 2015 to 2019, he was an Associate Scientist with the Biospheric Sciences Laboratory, NASA Goddard Space Flight Center, Greenbelt, MD, USA, where he worked on digital-beamforming-based radio frequency interference (RFI) mitigation techniques for synthetic aperture radar (SAR). Since 2019, he has been with the Microwaves and Radar Institute, German Aerospace Center (DLR), Wessling, Germany. His research interests include active microwave remote sensing, with special interest in SAR signal processing, performance simulation, digital beamforming, and RFI mitigation.

Dr. Bollian is a member of the IEEE Geoscience and Remote Sensing Society and a Co-Chair of the IEEE Geoscience and Remote Sensing Society (GRSS) Frequency Allocations in Remote Sensing Technical Committee.

Michelangelo Villano (Senior Member, IEEE) received the B.Sc. and M.Sc. degrees (Hons.) in telecommunication engineering from the Sapienza University of Rome, Rome, Italy, in 2006 and 2008, respectively, and the Ph.D. degree (Hons.) in electrical engineering and information technology from the Karlsruhe Institute of Technology, Karlsruhe, Germany, in 2016.

From 2008 to 2009, he was a Young Graduate Trainee with the European Space Research and Technology Center, European Space Agency, Noordwijk, The Netherlands, where he developed processing algorithms for ice sounding radar. In 2017, he was a Visiting Research Scientist with the Communications, Tracking, and Radar Division, NASA Jet Propulsion Laboratory, Pasadena, CA, USA, where he analyzed novel acquisition modes for the NASA Indian Space Research Organization synthetic aperture radar (SAR) instrument. Since 2009, he has been with the German Aerospace Center (DLR), Microwaves and Radar Institute, Wessling, Germany, where he is currently the Head of the New Space SAR Research Group. Since 2019, he has also been a Lecturer with Ulm University, Ulm, Germany. He has authored or coauthored more than 110 research articles in peer-reviewed journals and international conference proceedings. He holds ten patents in the field of SAR. His research interests include the conception of innovative SAR modes for high-resolution wide-swath imaging and the development of low-cost SAR solutions for frequent and enhanced Earth monitoring.

Dr. Villano has been a member of the Technical Program Committee of the European Conference on SAR (EUSAR), since 2016. He was a recipient of the First Place Student Paper Award at the EUSAR, Berlin, Germany, in 2014, the IEEE Geoscience and Remote Sensing Society Letters Prize Paper Award, in 2015 and 2017, the Student Paper Award at the Asia-Pacific Conference on Synthetic Aperture Radar, Marina Bay Sands, Singapore, in 2015, the DLR Science Award, in 2016, the Award as Young Scientist of the Foundation Werner von Siemens Ring, in 2017, the ITG Dissertation Award, in 2017, and the Best Paper Award at the German Microwave Conference 2019. He is Co-Chair of the Working Group on Remote Sensing Instrument and Technologies for Small Satellites of the IEEE Geoscience and Remote Sensing Society's Technical Committee on Instrumentation and Future Technologies. He is currently an Associate Editor for the IEEE Geoscience and Remote Sensing Letters. He was a Guest Editor for the special issues Advances in Antenna Array Processing for Radar 2014 and Advances in Antenna Array Processing for Radar 2016 of the *International Journal of Antennas and Propagation*.

Gerhard Krieger (Fellow, IEEE) received the Dipl.-Ing. (M.S.) and Dr.-Ing. (Ph.D.) (Hons.) degrees in electrical and communication engineering from the Technical University of Munich, Germany, in 1992 and 1999, respectively.

From 1992 to 1999, he was with the Ludwig Maximilians University, Munich, where he conducted multidisciplinary research on neuronal modeling and nonlinear information processing in biological and technical vision systems. Since 1999, he has been with the Microwaves and Radar Institute of the German Aerospace Center (DLR), Oberpfaffenhofen, Germany, where he started as a Research Associate developing signal processing algorithms for a novel forward-looking radar system employing digital beamforming on receive. From 2001 to 2007, he led the New SAR Missions Group which pioneered the development of advanced bistatic and multistatic radar systems, such as TanDEM-X, as well as innovative multichannel SAR techniques and algorithms for high-resolution wide-swath SAR imaging. Since 2008, he has been the Head of the Radar Concepts Department which hosts about 40 scientists focusing on new SAR techniques, missions and applications. He has moreover been serving as Mission Engineer for TanDEM-X and he made also major contributions to the development of the Tandem-L mission concept, where he led the Phase-0 and Phase-A studies. Since 2019, he is moreover a professor at the Friedrich-Alexander-University Erlangen, Germany. Gerhard Krieger is author or co-author of more than 100 peer-reviewed journal papers, 9 invited book chapters, more than 400 conference papers, and more than 20 patents. Prof. Krieger has been an Associate Editor for the IEEE Transactions on Geoscience and Remote Sensing since 2012. In 2014, he served as the Technical Program Chair for the European Conference on Synthetic Aperture Radar and as a Guest Editor for the IEEE Journal of Selected Topics in Applied Earth Observations and Remote Sensing. He received several national and international awards, including two Best Paper Awards at the European Conference on Synthetic Aperture Radar, two Transactions Prize Paper Awards of the IEEE Geoscience and Remote Sensing Society, and the W.R.G. Baker Prize Paper Award from the IEEE Board of Directors.

Dr. Krieger has been an Associate Editor for the IEEE TRANSACTIONS ON GEOSCIENCE AND REMOTE SENSING since 2012. He received several national and international awards, including two Best Paper Awards at the European Conference on Synthetic Aperture Radar, two Transactions Prize Paper Awards of the IEEE Geoscience and Remote Sensing Society, and the W.R.G. Baker Prize Paper Award from the IEEE Board of Directors. In 2014, he served as the Technical Program Chair for the European Conference on Synthetic Aperture Radar and a Guest Editor for the IEEE JOURNAL OF SELECTED TOPICS IN APPLIED EARTH OBSERVATIONS AND REMOTE SENSING.

Alberto Moreira (Fellow, IEEE) received the B.S.E.E. and M.S.E.E. degrees from the Aeronautical Technological Institute (ITA), São José dos Campos, in 1984 and 1986, respectively, and the Eng. Dr. degree (Hons.) from the Technical University of Munich, Germany, in 1993. From 1996 to 2001, he was the head of the SAR Technology Department, German Aerospace Center (DLR), Oberpfaffenhofen, Germany. Under his leadership, the DLR airborne SAR system has been upgraded to operate in innovative imaging modes like polarimetric SAR interferometry, tomography and holography. Since 2001, he has been the Director of the Microwaves and Radar Institute at DLR and a Full Professor with the Karlsruhe Institute of Technology (KIT), in the field of microwave remote sensing. His DLR's Institute contributes to several scientific programs and projects for spaceborne SAR missions like TerraSAR-X, TanDEM-X, Tandem-L, HRWS, SAR-Lupe and SARah as well as Kompsat-6, PAZ, Sentinel-1, BIOMASS, ROSE-L, Harmony, Sentinel-1NG, Envision and VERITAS. The mission TanDEM-X, led by his Institute, has generated a global, high-resolution digital elevation model of the Earth with unprecedented accuracy. He is the Initiator and Principal Investigator (PI) for this mission. His professional interests and research areas encompass spaceborne radar end-to-end system design, microwave techniques and system concepts, signal processing, and remote sensing applications. He is author or co-author of more than 450 publications in international conferences and journals, 8 book chapters, and holds more than 40 international patent grants in the radar and antenna field.

From 1996 to 2001, he was the Head of the SAR Technology Department, German Aerospace Center (DLR), Weßling, Germany. Under his leadership, the DLR airborne synthetic aperture radar (SAR) system has been upgraded to operate in innovative imaging modes, such as polarimetric SAR interferometry, tomography, and holography. Since 2001, he has been the Director of the Microwaves and Radar Institute, DLR, and a Full Professor with the Karlsruhe Institute of Technology (KIT), Karlsruhe, Germany, in the field of microwave remote sensing. His DLR's Institute contributes to several scientific programs and projects for spaceborne SAR missions, such as TerraSAR-X, TanDEM-X, Tandem-L, HRWS, SAR-Lupe and SARah, Kompsat-6, PAZ, Sentinel-1, BIOMASS, ROSE-L, Harmony, Sentinel-1NG, Envision, and VERITAS. The mission TanDEM-X, led by his institute, has generated a global, high-resolution digital elevation model of the Earth with unprecedented accuracy. From 2012 to 2018, he was the Principal Investigator for the Helmholtz Alliance "Remote Sensing and Earth System Dynamics" in support of Tandem-L, a radar mission proposal for the global observation of dynamic processes on Earth's surface with unprecedented quality and resolution. He is currently serving as a member of the Science Study Team for the ESA's mission EnVision. Since 2003, he has served as a member for several ESA Mission Advisory Groups, including ENVISAT/ASAR, Sentinel-1, and Hydroterra. He is the initiator and the principal investigator (PI) for this mission. He is the author or coauthor of more than 450 publications in international conferences and journals and eight book chapters. He holds more than 40 international patent grants in the radar and antenna field. His professional interests and research areas encompass spaceborne radar end-to-end system design, microwave techniques and system concepts, signal processing, and remote sensing applications.

Dr. Moreira served as President of the IEEE Geoscience and Remote Sensing (GRS) Society in 2010 as well as General Co-Chair of International Geoscience and Remote Sensing Symposium (IGARSS) in 2012. He was founder and chair of the GRSS German Chapter (2003-2008), served as Associate Editor for the IEEE GRS Letters (2003-2007) and for the IEEE TGRS (since 2005), and he has been serving as chair of the Major Awards of the GRS society, since 2017. He is recipient of several international awards including the IEEE AESS Nathanson Award (1999), the IEEE Kiyo Tomiyasu Field Award (2007), IEEE W.R.G. Baker Award from the IEEE Board of Directors (2012), and the IEEE GRSS Distinguished Achievement Award (2014). He and his colleagues received the GRSS Transactions Prize Paper Awards in 1997, 2001, and 2007 and the GRSS Letters Prize Paper Award in 2015 and 2017. From 2012 to 2018 he has served as principal investigator for the Helmholtz Alliance "Remote Sensing and Earth System Dynamics" in support of Tandem-L, a radar mission proposal for the global observation of dynamic processes on Earth's surface with unprecedented quality and resolution. He is currently serving as a member of the Science Study Team for the ESA's mission EnVision, and has served since 2003 as member of the several ESA Mission Advisory Groups including ENVISAT/ASAR, Sentinel-1 and Hydroterra.